GARNET ZONING PATTERNS RECORD MULTIPLE PROCESSES OF CHEMICAL TRANSFER DURING SUBDUCTION

Authors

Freya R. George*[1,2] (freya.george@bristol.ac.uk), Daniel R. Viete[2], Janaína Ávila[3,4], Gareth G.E. Seward[5], George L. Guice[2,6,7,8], Mark B. Allen[9], Michael J. Harrower[2,10]

Affiliations

[1] School of Earth Sciences, University of Bristol, Bristol, BS8 1RJ, UK
[2] Department of Earth & Planetary Sciences, Johns Hopkins University, Baltimore, MD 21218, USA
[3] School of Earth and Environmental Sciences, The University of Queensland, St Lucia QLD 4072, Australia
[4] Research School of Earth Sciences, The Australian National University, Canberra ACT 0200, Australia
[5] Department of Earth Science, University of California, Santa Barbara, CA 93106, USA
[6] Department of Mineral Sciences, Smithsonian National Museum of Natural History, Washington D.C., 20560, USA
[7] Department of Earth & Planetary Sciences, American Museum of Natural History, New York City, NY 10024, USA
[8] Department of Physics, Astronomy & Geosciences, Towson University, Towson, MD 21252, USA
[9] Department of Earth Sciences, Durham University, Durham, DH1 3LE, UK
[10] Department of Near Eastern Studies, Johns Hopkins University, Baltimore, MD 21218, USA

Abstract

Subduction facilitates the transfer of volatiles from the Earth's surface to its interior. However, the rock-scale processes that govern the efficiency of deep volatile transfer are not fully understood. Garnets from subduction zone rocks commonly have fine-scale, oscillatory elemental zoning that is typically considered to record external fluid ingress/transfer. Elemental and oxygen-isotope zoning in garnets from five exhumed subduction zone complexes show that in subduction zone rocks these records are not necessarily coupled; oxygen isotope evidence of ingress of buffering fluids, obvious only in rare cases, is decoupled from shorter length scale elemental and oxygen isotope zonings (which also show no coupling with each other). This finding suggests multiple mechanisms of internal chemical transfer operate at the grain and rock scale during subduction, and that rocks may commonly experience only limited interaction with external fluids. The results presented are consistent with a picture of volatile transfer in subduction that is spasmodic, highly localized, and variably efficient at evacuating fluids inherited from the surface then released by metamorphic dehydration.

Introduction

During subduction, prograde dehydration of oceanic lithosphere liberates large volumes of fluids. Understanding the fate of these fluids—released to the mantle wedge, mobilized up the slab–wedge interface, or transferred to sub-arc depths—is critical given their influence over arc magmatism, earthquake source processes, and mass transfer and chemical cycling between Earth's surface and interior (e.g., Schmidt and Poli, 1998; Collido et al., 2018). In high pressure–low temperature (*HP–LT*; eclogite and blueschist facies) metabasic rocks from subduction settings, garnet-bearing assemblages are common. Since first documented in Franciscan blueschists (Dudley, 1969), oscillatory chemical zoning (short-wavelength peaks and troughs in elemental concentration approximately parallel to the mineral interface) in *HP–LT* garnet has been recognized worldwide (e.g., García-Casco et al., 2002; Kabir and Takasu, 2010; Li et al., 2016). This includes garnet-bearing rocks from subduction zones that differ with respect to their bulk composition, relative *P–T* path of metamorphism and age, and from regions with and without obvious fluid channelization features (Hoover et al., 2022). Given the widespread occurrence of oscillatory zoning in *HP–LT* garnet, it is likely to record some fundamental process (or processes) that operate(s) at garnet-stable conditions in subduction zones.

Owing to the demonstrable relationship between fluid infiltration and oscillatory elemental zoning in minerals from other fluid-rich geological settings—including andradite garnet from hydrothermal skarns and contact aureoles (e.g., Jamtveit et al., 1995, Stowell et al., 1996) and pyroxenes and garnet in mineralized shear zones and metasediments (Yardley et al., 19991; Schumacher et al., 1999)—oscillatory zoning in *HP–LT* garnet is often attributed to pulsed metasomatic changes to the composition of the grain boundary during garnet growth (e.g., Hickmott et al., 1992, Angiboust et al., 2014). Indeed, oscillatory zoning in garnet formed at high pressure in coarse, fluid-filled porosity has been associated with processes of metamorphic dehydration (Angiboust and Raimondo, 2022).

Despite evidence for long-range transfer of subduction-related fluids through deformation-induced conduits (e.g., Breeding et al., 2004; Spandler et al., 2011), mechanisms responsible for grain-scale fluid and element transfer in intact and nominally impermeable eclogites and blueschists remains poorly understood. In particular, debate surrounds whether the principal mode of fluid transfer through these rocks is via: (1) flow within an interconnected porosity driven by small- to large-scale gradients in stresses (e.g., Connolly and Poladchikov, 2004; Bovay et al., 2021); or (2) channelized transfer through, for example, veins produced by dehydration embrittlement (Camacho et al., 2005; John et al., 2012; Taetz et al., 2018), a reactive porosity (Plümper et al., 2017) or compaction channels (Piccoli et al., 2021). Whether the observed elemental oscillations in *HP–LT* garnet record fluid infiltration during subduction will depend, in large part, on mechanisms of fluid transfer at the grain scale as well as the buffering capacity of infiltrating fluids.

Assessment of the potential role of grain-scale fluid transfer processes has been made possible by increased analytical capabilities of stable isotope approaches (e.g., Taetz et al., 2012; Gerrits et al., 2019; Penniston-Dorland et al., 2019). In particular, *in situ* measurement of the oxygen isotope composition ($\delta^{18}O$) of metamorphic minerals enables constraints to be placed on the sources and pathways of reactive fluids present during mineral re-crystallization (e.g., Vielzeuf et al., 2005; Scicchitano et al., 2022). Relatively cool subduction zone geotherms coupled with slow oxygen diffusivities (e.g., Higashini et al., 2019) ensure that $\delta^{18}O$ variations at scales of <10–100 μm in garnet are rarely modified by diffusion at *HP–LT* conditions, offering a faithful record of prograde processes in eclogites and blueschists (Russell et al., 2013). Consequently, oxygen isotopes can provide constraints on metamorphic fluid histories in subduction zones that are inaccessible from the elemental record alone. Long wavelength core-to-rim $\delta^{18}O$ variation in garnet has been associated with influx of external fluids with distinct isotopic signatures, with positive shifts (~2.5–4‰) attributed to influx of

isotopically-heavy, sediment-derived fluid into high-*P* boudins (Russell et al., 2013) and via channelization in metasomatized rocks (Rubatto and Angiboust. 2015). Moreover, shifts to lower $\delta^{18}O$ values (by ≤ 8‰) attributed to infiltration of isotopically-light, serpentinite- or altered gabbro-derived fluids on either the prograde (Martin et al., 2014; Bovay et al., 2021) or retrograde path (Page et al., 2014, Cruz-Uribe et al., 2021).

Here, we utilize *in situ* measurements of major and trace elements and oxygen isotopes at the scale of individual growth zones to test the hypothesis that oscillatory zoning is demonstrably linked to repeated episodes of fluid infiltration and metasomatism. The oxygen isotope results reported do not show obvious indication of external fluid ingress, casting doubt on the notion that short wavelength elemental oscillations are, in all cases, genetically related to repeated fluid infiltration. However, observed isotopic variation in garnet across multiple wavelengths does shed light on two end-member mechanisms of grain boundary fluid transfer during *HP–LT* metamorphism. Our new data do not suggest that most reactive *HP–LT* systems are exposed to externally-derived fluids during prograde garnet crystallization. Differences in isotopic patterns within and across garnet grains may be explained by temporally-variable grain boundary porosity and permeability, resulting in evolving connectivity of locally sourced and isotopically heterogeneous internal fluids. Transient open-system infiltration of isotopically and chemically buffering fluids, as has been previously documented, may represent the (spatially integrated) exception rather than the norm in these *HP–LT* metabasic systems.

Methodology

Garnet-bearing *HP–LT* metabasites from five subduction zones were selected to capture some of the global heterogeneity within this tectonic setting. Each has been studied extensively by previous authors, yielding good constraints on conditions of peak metamorphism and relative *P–T* paths during subduction. Representative samples are derived from *HP–LT* metabasic blocks in block-in-mélange settings, and include: amphibolite–eclogite from As Sifah (Oman; OM18-03) and Puerto Cabello (Venezuela; VE13-11), interlayered blueschist–eclogite from the Cycladic Blueschist Unit, Syros (Greece; SY15-10) and the Franciscan Complex, California (USA; CA13-01), in addition to core and rind samples from a lawsonite eclogite block of the Samana Complex, Punta Balandra (Dominican Republic; SS85-27E and SS85-27BC, respectively). Other than the samples from the Dominican Republic, were obtained from outcrop and, except for the Oman samples, were not demonstrably associated with prograde fluid focusing structures or shear zones. However, in each case, the *HP* metamorphic matrix assemblage has been modified by post-peak mineral growth. It is beyond the scope of this work to fully model the *P–T* evolution of each sample in detail, but constraints on *P–T*–time (*t*) conditions of metamorphism in addition to photomicrographs of each sample are provided in Table 1 and Figure 1, with full details in Supplementary Material (SM) 1.

Across rims of several garnets from each sample, co-located transects for major elements and oxygen isotopes were acquired, using electron probe microanalyses (EPMA) at the University of California, Santa Barbara (USA) and the University of Ottawa (Canada), and secondary ionized mass spectrometry (SIMS) on the Sensitive High Resolution Ion Microprobe–Stable Isotope (SHRIMP–SI) at the Australian National University. Laser ablation–inductively coupled plasma–mass spectrometry (LA–ICP–MS) mapping was conducted on garnet from Oman at Johns Hopkins University (USA). Full details of the analytical methods are provided in SM 2.

Results

Major and trace element zoning in garnet

Multiple representative EPMA X-ray Mn maps from each *HP–LT* setting are presented in Figure 2, and background corrected maps of Mg, Fe, Ca, Mn, and Al content for all 16 mapped garnets are presented in SM 3. All garnets display grain-scale core-to-rim decreases in Mn content and increases in Mg content. In mantle to rim regions, porphyroblasts contain concentric oscillatory/rhythmic major element zoning that is most pronounced in Mn and sometimes evident in Mg. Though the general form of the oscillations—interface-parallel peaks and troughs with a resolvable wavelength of 20–100 μm and an amplitude of 0.25–1.5 mol% spessartine—is the same for all settings, in detail, their magnitude, positioning and number varies from setting to setting. The Ca and Fe maps (the two most abundant divalent cations in these garnets) do not exhibit clear oscillations. In places, the Ca zoning hints at patterns parallel to oscillations in Mn, but the dominantly patchy and non-concentric Ca distribution may record kinetic inhibition and chemical disequilibrium, as suggested in other studies (e.g., George et al., 2018).

Mn zoning in garnet from sample OM18-03C typifies the form of oscillatory zoning investigated in this study. It is present across the outermost 300–500 μm of garnet (Fig. 2a), rim-wards of a broad core-to-mantle decrease in the spessartine content. Garnets in OM18-03B, collected from the same location (2 m apart) and with an equivalent assemblage, contain narrower oscillatory regions and a different sequence of peaks and troughs (Fig 2b; SM 3). For a given Oman hand sample, equivalent oscillations can be tracked among garnet grains of the same thin section, and in both OM18-03B and -03C the onset of short-wavelength oscillations is associated with a sharp increase in average Mn and Ca contents (by ~1 mol.% and ~11 mol.%, respectively), and a decrease in the average Fe content (Fig. 2a, b; SM 3). The Mn maps in all Venezuelan garnets from VE13-11 exhibits single, ~35 μm-wide mantle peaks succeeded by three near-rim vacillations in rim regions that contain lower Mn and Fe and higher Mg (Fig. 2c, d; SM 3). In the three Greek garnets from SY15-10, all grains exhibit a 50–70 μm wide oscillation in Mn content (Fig. 2e, f; SM3). In Californian garnets from CA13-01, oscillations occur in the outermost 250–300 μm of the rims (Fig. 2g–i) and and are widest (~70 μm) towards the core. In the two mapped Dominican Republic rind garnets from SS85-27BC1, 10–50 μm-wide oscillations—again equivalent across different grains—are superimposed on a near-rim shoulder in Mn and a narrow outer-rim region containing lower Mg and Ca, and high Fe content (Fig. 2j; SM 3). In the smaller garnet from the core of the same block (sample SS85-27E), three ~100 μm-wide Mn peaks are identifiable (Fig. 2k, SM 3).

These maps indicate that, for any given *HP–LT* sample, primary major element oscillations across multiple garnet grains exhibit common radial positioning, and amplitudes that are independent of grain size. Converse to this finding of apparent thin-section scale equilibration, samples collected within several meters of each other across an outcrop or between core and rind, as in Oman and the Dominican Republic, respectively, exhibit differences in the precise positioning of fine-scale oscillations but not in grain-scale step changes in average elemental composition.

Corresponding LA–ICP–MS maps of trace elements in garnet from OM18-03 reveal a diverse suite of zoning patterns, variably correlated with major element distributions. Light to heavy rare earth elements (L–HREE) and Y exhibit oscillations that are spatially coincident with those preserved in Mn, but which sometimes differ in terms of whether they exhibit positive or negative excursions (Fig. 3a–c; SM 4). With the exception of Lu, oscillations are generally less pronounced from HREE to LREE, and Y and HREE indicate that elemental oscillations occur more core-ward than revealed by the major-element EPMA maps alone (Fig. 3a, b; SM 4).

Changes in the oxidation state of the reactive bulk composition modifies the Fe^{3+}–Al octahedral site ratio incorporated into garnet during its growth (a substitution less dependent on temperature, pressure, pH, and

salinity in garnets containing X_{grs}<0.4; Jamtveit et al., 1995). The andradite content of garnet in this study is <1–4 mol%, consistent with the typical range reported in *HP–LT* metamorphic garnet (cf. Gerrits et al., 2019). Garnet in CA13-01, SS85-27BC1, SS85-27E, VE13-11, and SY15-10 exhibit no systematic Al or andradite zoning across regions of elemental oscillations (Fig. 4c–k; SM 3). However, unlike all other garnet mapped in this study, grains from both OM18-03B and -03C exhibit near-rim concentric increases in Al content (Fig 3e; SM 3), and associated rim-ward declines in the andradite content, from 4 mol% to 2 mol% (Fig. 4a, b). These boundaries are coincident with pronounced changes in average Mn, Fe, and Ca content (SM 3). A change in concentration of redox-sensitive trace elements (V, Co, Eu and Cr) also coincides with this mapped change in Fe^{3+}–Al substitution (Fig. 3c–e; SM 4). Though only subtly expressed on linear plots of concentration, this boundary also marks an inflection point across which the average rim-ward gradient in Y, Dy, Sc—all elements present in relatively high (>30 ppm) concentrations—inverts from negative to positive (Fig. 3a).

Oxygen isotope zoning in garnet

The positioning of SIMS oxygen isotope analysis transects of garnet was chosen based on the distribution of Mn oscillations and are shown as spots in Figure 2 and core–rim profiles in Figure 4. For nine of the 11 SIMS-analyzed garnets, two SIMS transects were collected; given the axial symmetry in oscillatory Mn zoning, data are plotted as distance from the outer rim (Fig. 4). Full data for individual measurements are provided in SM 5.

In the cores of garnet porphyroblasts from all settings, $\delta^{18}O$ generally exceeds 5.5‰. These values of core $\delta^{18}O$—~5.6‰ in Venezuela, ~7.5‰ in Greece, 8.5–9.3‰ in California, 10–11.5‰ in the Dominican Republic and 11–12‰ in Oman—are interpreted to reflect inheritance of the $\delta^{18}O$ signature derived from variable degrees of low-*T* hydrothermal alteration of an oceanic crust protolith (with primary MORB $\delta^{18}O$ ~5.5‰), rather than reflecting prograde metamorphic processes (Russell et al., 2013, Putlitz et al., 2000). A contribution to the differences in absolute $\delta^{18}O$ may also derive from isotope fractionation at different temperatures at the onset of garnet growth in each rock/setting (e.g., Kohn et al., 1993; Vho et al., 2020). Rim-ward of cores, distinct $\delta^{18}O$ zoning patterns incorporate features preserved over two distinctly different wavelengths.

At the sub-grain scale (100–500 μm), garnets exhibit intragrain $\delta^{18}O$ variation characterized by 50–300 μm-wide ≲1–2‰ 'saw-tooth' vacillations that exceed the internal uncertainty on individual analyses (Fig. 4). For example, in a rind garnet from the Dominican Republic (SS85-27BC1), internal $\delta^{18}O$ variation defines three coherent and symmetrical ~11‰ peaks in $\delta^{18}O$ across a radial distance of ~1200 μm, with $\delta^{18}O$ repeatedly returning to values of ~9.5‰ rim-ward of each peak (Fig. 4j). Unlike the oscillatory zoning in major elements, which is relatively uniform across and among grains from a single thin section, this intragrain oxygen isotope zoning in garnet differs among garnets from the same thin section; for example, in SY15-10B garnet 5, $\delta^{18}O$ exhibits a gentle increase from the core then a sharp decrease ~100 μm from the rim (Fig. 4e), whereas $\delta^{18}O$ in SY15-10B garnet 1 exhibits very slight changes in the gradient of zoning at an equivalent distance from euhedral rims (Fig. 4f). Average $\delta^{18}O$ in rims of all Californian garnets is similar (9 ± 1‰), but intra-grain zonation and rim values are spatially heterogenous (within a grain) and different among grains; for example, CA13-01 garnet 2 (Fig. 4g) exhibits asymmetry across the core, with one rim exhibiting only minor spot-to-spot change on the order of 1‰ and the other displaying internal variation up to ~2‰, whereas $\delta^{18}O$ zonations in both CA13-01 garnet 1 (Fig. 4h) and CA13-01 garnet 3 (Fig. 4i) are near symmetrical about their respective cores, with comparable near-rim internal $\delta^{18}O$ structure.

At the grain scale (≥1000 μm), the $\delta^{18}O$ patterns are different. In samples from Venezuela, Greece and the Dominican Republic, the internal and short-wavelength $\delta^{18}O$ vacillations are superimposed on flat (~0‰) to a 1–1.5‰ overall *net* $\delta^{18}O$ increase across cores to rims of garnet (Fig. 4c–f, j, k). Garnets from California also

exhibit uniform to slightly increasing interior $\delta^{18}O$, if the anomalously low $\delta^{18}O$ points in the outermost rim of garnets 1 and 3 are ignored (Fig. 4g–i). Garnets from Oman have the highest core $\delta^{18}O$ (11–12‰), with a similar slight increase to values of 12–13‰. However, rim-ward of these maxima, $\delta^{18}O$ vacillations in OM18-03B and -03C are superimposed on a longer wavelength net decrease in $\delta^{18}O$ of 2.5–4‰ (Fig. 4a, b) that seems to flatten in the outermost rim (Fig. 4b). Garnets from Oman, derived from similar samples collected two meters apart at a single outcrop have isotopic compositions at their rims that differ by ~2‰.

No discernible covariance in $\delta^{18}O$ and cation zoning

As the most pronounced component in which oscillations are documented, the Mn content is hereafter used as the principal comparative element to determine if isotopic changes are associated with elemental changes in garnet. Analysis of linear covariance between $\delta^{18}O$ and spessartine content suggests no (positive or negative) coupling between the two datasets across oscillatory zoned regions of any grain (Table 2). Correlation coefficients (r-values) calculated for the $\delta^{18}O$ and corresponding spessartine were also calculated along each profile. Generally, these exhibit moderate and negative r-values. In most cases, these are not significant at the 95% confidence level, but in the cases of OM18-03C and SY15-10B there is a statistically significant negative correlation (Table 2). However, rather than relating to coincidence between Mn and $\delta^{18}O$ zoning at the intragrain length scale, we consider it likely that these apparent correlations result from the strong fractionation-controlled core-to-rim decrease in Mn content and the slight net core-to-rim increases in $\delta^{18}O$. Assessment of correlations between the magnitude of fluctuations from point to point, which may be expected to be significant if the two datasets vary at the same wavelength, are not significant in any grain.

Principal component analyses (PCA) performed for combined mantle and near-rim regions of grains from a given locality (details of approach provided in SM 3) similarly highlight the absence of any systematic covariance between spessartine and $\delta^{18}O$ (Fig. 5); in addition, no other garnet end-member consistently exhibits correlation with $\delta^{18}O$. As with statistical approaches, empirical assessment of the covariance between elemental maps and isotopic spots across oscillatory rims in Fig. 2 indicate that there is not a spatial coincidence between the positioning of elemental oscillations and internal short wavelength intragrain variation of $\delta^{18}O$.

Though garnet from several settings contain pronounced near-rim changes (in both grains from Venezuela and the outermost rim of SS85-27BC1), the only evident correlative record between oxygen isotope compositions and elemental compositions occurs in garnet from Oman. In these samples, long wavelength, rim-ward decreases in $\delta^{18}O$ are spatially coincident with declines in the andradite content and pronounced changes in average major and trace element concentrations (Fig. 4a, b; SM 3, 4). Andradite reference standards were monitored during analyses (and calibrations checked) and suggest that the matrix bias effect had negligible impact on this change. At the X_{And} of relevance (<0.04) the additional $\delta^{18}O$ matrix correction is ~0.2 (consistent with that calibrated Martin et al., 2014). Interestingly, and based on LA–ICP–MS maps of OM18-03C, the position of this sharp boundary (Fig. 3a) is not coincident with the core-most garnet radius at which oscillations are detectable in the Y and REE content (i.e., small-wavelength elemental vacillations are evident in both isotopically distinct—core and rim—domains).

Summary of elemental and oxygen isotopic zoning observed in the *HP-LT* garnets

1. Small-wavelength oscillations are observed for Mn in the mantle and rim regions of all garnets studied. These Mn zoning patterns are associated with Mg in some samples. Where L–HREE and Y were also mapped, these elements covary with Mn. Elemental zoning patterns are approximately axisymmetric in all grains studied and are equivalent for all garnets on at least the hand sample scale.

2. Unlike the elemental zoning patterns, small-wavelength oscillations in $\delta^{18}O$ are not axisymmetric and vary among grains separated by mm to cm length scales. Qualitative analysis and PCA reveal zero spatial coincidence (coupling) among short wavelength elemental oscillations and $\delta^{18}O$ variations.

3. In the Oman garnets, larger-wavelength variations in chemistry (upon which the shorter-wavelength records are superimposed) are revealed by grain-scale Al (andradite) variation and changes in $\delta^{18}O$ not observed in garnets from any of the other samples. This zoning is demonstrably coupled to variation in other redox-sensitive elements (V, Co, Eu, Cr), in addition to trace elements/REE (Y, Dy, Sc). This longer-wavelength chemical zonation seen only in the Oman garnet is the only zoning feature for which elemental and isotopic concentrations covary.

Discussion

Results presented here demonstrate the coexistence of short-wavelength elemental oscillations and saw-tooth intra-grain oxygen isotope variations in *HP-LT* garnet, but that these signals are decoupled. There is no evidence in our data to link oscillatory elemental zoning in *HP–LT* metabasic garnet to pulsed infiltration of isotopically-distinct grain boundary fluids that buffer garnet chemistry—as has been suggested for some shallower fluid-rich settings (e.g., Jamtveit at al., 1995; Yardley et al., 1991) and in eclogitic vein garnet (e.g., Spandler et al., 2011; Angiboust and Raimondo, 2022).

Though the total range in internal $\delta^{18}O$ variation in garnet nears 2‰ in some garnet, the *net* core-to-rim variation in all garnet from the Dominican Republic, California, Venezuela, and Greece is $\leq 1 \pm 0.3$‰. Modest (0.2–1‰) core-to-rim increases in the $\delta^{18}O$ of garnet have been previously shown to result from mineral fractionation, dehydration reactions, and fluid loss over a temperature evolution of 100–200 °C (Kohn et al., 1993; Vho et al., 2020). The net core-to-rim variation documented in the garnets studied is consistent with crystallization of these garnets in overall closed systems. Conversely, in the garnets from Oman, a dramatic change in major and trace element concentration is coupled to a near-rim 2.5–4‰ decrease in $\delta^{18}O$, a magnitude exceeding that anticipated for prograde garnet crystallization in a closed system (Kohn et al., 1993; Vho et al., 2020). These coupled, long-wavelength (grain-scale) zoning records are interpreted to reflect opening of the grain boundary network to externally-derived, isotopically-, and chemically-distinct buffering fluids (Fig. 5).

In the following text, we discuss: (a) the potential origin of small-wavelength $\delta^{18}O$ vacillations in all samples; (b) the magnitude, composition, and source of fluids that buffer garnet compositions in Oman; and (c) mechanisms (alternative to external fluid ingress) by which oscillatory elemental zoning may be incorporated in garnet during prograde growth. Discussion points (a), (b) and (c) relate directly to points 2, 3 and 1, respectively, listed in the summary of the Results section.

(a) Origin of the short-wavelength oxygen isotope vacillations

In all settings (including Oman), intra-garnet $\delta^{18}O$ variations point to temporal heterogeneity in the isotopic composition of the grain boundary fluid in systems that do not obviously record open-system conditions over the duration of garnet crystallization. Cross-porphyroblast asymmetry of the $\delta^{18}O$ vacillations in some garnets (Fig. 3), in addition to grain-to-grain heterogeneity in $\delta^{18}O$ zoning, also alludes to significant mm- to cm-scale spatial heterogeneity in the distribution of ^{16}O versus ^{18}O in the grain boundary during mineral growth. In contrast, elemental zoning is typically equilibrated over the same length scales.

From where then do these spatiotemporal heterogeneities in $\delta^{18}O$ arise? As hypothesized by Russell et al. (2013), saw-tooth variations may indicate fluxing of higher and lower $\delta^{18}O$ fluids through the grain boundary network, derived from alternating (external) sedimentary and mafic sources. Such a scenario would require transient passage of fluids that do not impart a lasting isotopic signature in the rock (i.e., are rock buffered) yet maintain fluid compositions that are out of equilibrium (i.e., not rock buffered) over their transfer distances, which may be significant. Moreover, a scenario of garnet crystallization at high pressure while attached to the down-going slab rather than the mélange, would require underlying sedimentary sources to feed the slab-normal (or up-dip) migration of relatively high-$\delta^{18}O$ fluids, which is a difficult architecture to account for.

With the apparent difficulty of explaining short-wavelength $\delta^{18}O$ variations (decoupled to short-wavelength elemental zoning) in terms of external fluid ingress, we focus on potential explanations related to processes internal to the rock volume. Specifically, we target a mechanism that may result in significant internal heterogeneity in the $\delta^{18}O$ of fluids.

Vacillations in $\delta^{18}O$ may be facilitated by cyclic porosity–permeability variations that result in changes in local connectivity. Experimental constraints suggest that high dihedral angles (62°–68°) facilitate the evolution of isolated fluid pockets in HP rocks (Mibe et al., 2003). In such systems, heterogeneous, rock-wide variations in $\delta^{18}O$ of the grain boundary fluid may develop in response to, for example, spatially variable reaction–dehydration extent across the mm-to-cm scale or the evolution of extreme disequilibrium in fluid pockets. Abrupt and heterogenous breakdown of low-T phases (e.g., lawsonite or albite) may also drive local changes in the fluid $\delta^{18}O$. The fluids contained within a non-interconnected porosity may then become transiently and variably interconnected during deformation and/or porosity development (e.g., Holness, 1993), a process potentially enhanced along grain boundaries with favorable crystallographic misorientations. This would result in grain-scale to thin section-scale isotopic variations (reflecting rock-scale spatial heterogeneity in reaction progress) across the surfaces of growing garnet. This scenario is consistent with the hypothesis that old $^{40}Ar/^{39}Ar$ ages result from closed grain boundaries, allowing for accumulation of radiogenic Ar (e.g., Warren et al., 2011; Smye et al., 2013) and are consistent with reports of isolated fluid pockets at *HP–LT* conditions (Angiboust and Raimondo, 2022). It may also imply that a crustal scale recycling budget dominated by volatile solubility in serpentinite may be supplemented with volatiles preserved in stagnant—yet spatially and temporally heterogeneous—grain boundary pore space of mafic eclogite and blueschist.

Scenarios of heterogeneous porosity–permeability may facilitate locally channelized (at the scale of the grain boundary) porous flow. For example, fluid–solid dihedral angles may vary locally (e.g., Holness, 1993), particularly if large differential stresses are sustained across grains (Tajčmanová et al., 2014), resulting in a heterogeneous distribution and transfer of fluid that is also modified by porosity increases and fluid production during prograde metamorphic reaction (Fig. 6A–C). Alternatively, as with changes to the stress field in shallow systems (Elkhoury et al., 2006), down-dip transfer of dynamic seismic effects to garnet-stable parts of the subduction zone may induce episodes of enhanced permeability. In such cases, mechanical disruption associated with rigid grain interaction may induce porosity nucleation. Upon 'opening' of non-interconnected porosity, grain-scale channelization of aqueous fluid between domains containing discrete $\delta^{18}O$ may be driven by local gradients in fluid pressure and potential gradients that are then maintained during coupled reaction–transport processes (Plumper et al., 2017). In summary, it is not clear exactly what the short-wavelength $\delta^{18}O$ vacillations record, but it is possible that they are associated with a scenario of rapidly changing porosity–permeability linked to episodic processes in the dynamic subduction zone environment.

(b) Buffering of elemental and isotopic signatures at long length scales by external fluids

It is not possible to definitively exclude the possibility that external fluid infiltrated during garnet growth in all studied samples. For example, if infiltrating fluids had similar chemical and isotopic compositions to the country rock or very rapidly equilibrated with the oxygen already in the rock volume, external fluid ingress may leave no observable isotopic signature. However, samples from Oman provide the only clear, spatially-coupled evidence for significant modification of the effective bulk composition by isotopically-and chemically-distinct fluids. The discrete, 2.5–4‰ near-rim declines in $\delta^{18}O$ in the Oman garnet are comparable to changes interpreted to result from open system metasomatism in previous studies (e.g., Russell et al., 2013; Rubatto and Angiboust, 2015; Martin et al., 2014; Bovay et al., 2021), and are interpreted to reflect ingress of external fluids (Fig. 6). At this boundary, the corresponding decrease in the calculated andradite component of garnet, by 2–3 mol%, indicates that open system fluid infiltration during garnet mantle–rim growth may have been associated with a reduction of the reactive bulk fO_2 relative to the growth environment for core regions. A rock-wide increase in $Eu^{2+}/\sum Eu$ linked to reduction of the reactive bulk fO_2 may also explain the documented decline in Eu concentration at this boundary (Fig. 2C).

Owing to their large partition coefficients in garnet, steep decreases in the concentration of MREE and HREE rim-ward of core regions are expected to result from Rayleigh fractionation, with closed chemical systems yielding strongly depleted rims. However, in addition to an enrichment of the reactive bulk composition in Ca and Mn, the decline in andradite and $\delta^{18}O$ in Oman garnet is accompanied by subtle rim-ward increases in Dy, Gd and Lu content. This is consistent with recent experiments that have suggested that REEs may be mobilized in aqueous fluids at high pressure (Tsay et al., 2017). Experimental constraints attest to significant fluid mobility for Cr (Kogiso et al., 1997; Kessel et al., 2015), in agreement with a fluid-buffered increase in the average Cr concentration in the mantle–rim regions of the Oman garnets (Fig. 2E). Walters et al. (2021) recently suggested that Co budgets are dominated by reactions among Fe–Mg silicate phases, but here, a buffered increase of the Co concentration in the grain boundary by the proposed fluid infiltration event may suggest significant mobility of Co in subduction zone fluids.

Source and volume of external fluids recorded in the Oman garnets

Quantitative isotopic and thermodynamic modelling was conducted to explore the volume of fluid required to drive the observed isotopic changes in garnets from Oman. Although the bulk rock oxygen isotope composition of the Oman eclogites is unknown, it can be reconstructed with knowledge of mineral $\delta^{18}O$, modal abundances of the equilibrium assemblages at the conditions of garnet growth, and isotope fractionation factors among coexisting phases (e.g., Vho et al., 2020). Here, retrogressed matrix assemblages preclude the use of measured bulk rock compositions and the bulk $\delta^{18}O$. Instead, a generic altered mid-ocean ridge basalt (MORB) composition of Staudigel et al. (1996) is used to represent the primary elemental composition of the Oman eclogites. Full details of the modelling approach are provided in SM 2.

Using the PTloop 1.0 software and the database DBOXYGEN 2.0.3 (Vho et al., 2019, 2020), an original bulk $\delta^{18}O$ of ~14‰ is calculated as being in equilibrium with an average garnet core composition of ~12‰ at 480–550 °C. In the same temperature range, pure water with a $\delta^{18}O$ of 10.5–13‰ would be in equilibrium with the range of Oman garnet rim values of 9–10.5‰. Consequently, the decline in $\delta^{18}O$ in the rims of Oman garnet is likely to have been due to infiltration of an external fluid with a $\delta^{18}O$ of 10.5–13‰ or lower. Whether the difference in rim compositions between samples from the same outcrop is due to differences in the $\delta^{18}O$ of fluid at given fluid–rock ratios, or to spatially-variable fluid–rock ratios with a single fluid composition is unknown.

Several fluid sources can account for the core–rim $\delta^{18}O$ change observed in Oman garnet. In Oman, high-temperature serpentine contains $\delta^{18}O$ of 4–7‰ (Scicchitano et al., 2021). At temperatures of garnet mantle–rim growth (500–550 °C), the 1–2 wt.% fluids released from serpentinites with $\delta^{18}O$ of 5‰ is calculated to have a $\delta^{18}O$ of around 6.5–6.9‰. Alternatively, heavier $\delta^{18}O$ fluids (9–16‰) derived from sedimentary sources with bulk $\delta^{18}O$ of 14–26‰ (Bebout and Barton, 1989) may have driven the observed decline in $\delta^{18}O$ in the Oman garnet. Lastly, lawsonite, containing 11.5 wt% H_2O, liberates significant volumes of heavy $\delta^{18}O$ fluid (>14‰) during prograde metamorphic dehydration. Previous work has suggested that fluid release associated with lawsonite breakdown may be associated with a reduction of fO_2 of the residual assemblage, and a concomitant decline in the andradite component incorporated in garnet (Gerritts et al., 2019).

We explore the above scenarios to investigate potential fluid–rock ratios experienced by the Oman eclogites. Phase relations and isotope fractionation in altered MORB with an initial $\delta^{18}O$ of 14‰ were simulated along a *P–T* path from 1.4 GPa and 375 °C to 2.0 GPa and 550 °C (Fig. 7A). In a closed system, internally-produced H_2O volume increases to ~14 vol% after conditions of lawsonite dehydration, but $\delta^{18}O$ in garnet changes by only ~0.5‰ over the modelled path (Fig. 7A, B). External fluid infiltration is also simulated to occur in a single episode at 500 °C. By varying the mass of infiltrating fluid, fluid–rock ratios required to shift the $\delta^{18}O$ composition in growing garnet—from ~12.5‰ in the core to 9–10.5‰ in the rim—were evaluated.

For serpentinite-derived fluids ($\delta^{18}O$ of ~6.7‰), time-integrated infiltration of 6.6×10^4–1.3×10^5 kg of H_2O is required to reduce garnet $\delta^{18}O$ by 2–3.5‰, yielding fluid–rock mass ratios of 0.2–0.4 (Fig. 7C). In the case of isotopically-heavier sediment-derived fluids ($\delta^{18}O$ of ~12.5‰), greater volumes of fluid are required to buffer the same change in garnet composition: at least 2×10^6 kg of H_2O and fluid–rock mass ratios >6 are required (Fig. 7D). The effect of lawsonite dehydration on garnet $\delta^{18}O$ is negligible (see discussion in SM 2). Given evidence that these isotopic compositions in garnet did not equilibrate at the thin section scale and the assumption that fluids had not equilibrated with isotopically heavier crustal components during transfer, these estimated fluid–rock ratios likely represent minimum values. The calculated values yield time-integrated fluxes of 1.0–1.65×10^4 cm^3/cm^2 for serpentinite-derived fluids and $>2.0 \times 10^5$ cm^3/cm^2 for sediment-derived fluids, respectively, both at or exceeding the threshold of 10^4 cm^3/cm^2 for open system fluid transfer (Zach and John, 2007).

While most likely related to infiltration of external fluids derived from lithologically distinct units, the heavy average $\delta^{18}O$ in the cores of Oman garnet does not unequivocally distinguish a fluid source. Associated variation in elemental chemistry offers additional constraints: antigorite-derived fluids are generally enriched in Ca, Cr and LREE–MREE (Spandler et al., 2011, Spandler et al., 2014; Pettke & Bretcher, 2022), so the elemental changes associated with the fluid infiltration boundary in the Oman garnets (Fig. 1 and SM 3) may attest to an origin related to the infiltration of isotopically lighter, ultramafic-derived fluids. Such fluids are also anticipated to be enriched in, for example Li, B, LILE, Sb, U, and Sr; however, where measured with LA–ICP–MS, these masses are not documented to change in garnet at the corresponding boundary (SM 4). We consider it most likely that this relates to lack of strong fractionation of these elements between garnet and the fluid phases, rather than their absence in the fluid, and suggest assessment of other prograde phases may help to constrain this elemental budget.

(c) Potential origin of the short-wavelength elemental vacillations

Spatially associated but decoupled short wavelength $\delta^{18}O$ variation and elemental oscillations in garnet require that the driver of each short-wavelength zoning pattern (elemental v. oxygen isotopic) act simultaneously, yet possibly independently. The apparent decoupling of the records is inconsistent with the notion that fluctuating

elemental concentrations are driven by intermittent pulses of fluid-buffered change to the effective grain boundary chemistry (e.g., Jamtveit et al., 1995; Yardley et al., 1991; Tamblyn et al., 2020). Long-range fluid transfer events, as proposed to explain the longer-wavelength zoning feature in the Oman garnets, seem to exert little influence on the underlying process(es) driving the elemental oscillations, which are recorded both prior to and after first evidence of open system behavior in the OM18-03 samples (Fig. 6B versus Fig. 6C–E). The consistency of the radial positioning and amplitude of major element oscillations between grains of a given sample indicate that nutrient uptake was equilibrated at least at the mm to cm scale, in pronounced contrast to cross-porphyroblast disequilibrium in short wavelength $\delta^{18}O$ zoning in the same grains.

While it is beyond the scope of this study to discuss in detail what process—if not fluid buffering—oscillatory zoning may have been driven by, several alternative explanations have been proposed. Chemical oscillations have been linked to intermittent mineral breakdown (e.g., Konrad Schmolke et al., 2008; Hyppolitto et al., 2019). This would require rapid rock-wide chemical equilibration of liberated components, potentially at odds with the emerging picture of limited connectivity through the grain boundary network at high pressure (e.g., Angiboust and Raimondo, 2022). Complex mechanical cycling of material across and along the slab–mélange interface may drive equilibrium responses to *P–T* fluctuations (e.g., García-Casco et al., 2002; Blanco-Quintero et al., 2011; Tan et al., 2020), though the preservation of steep chemical gradients in Mn zoning in garnet may preclude physical processes that operate over tens of millions of years (Viete et al., 2018). Alternatively, Viete et al. (2018) proposed that oscillatory zoning may record pore fluid pressure (and related *P–T*) fluctuations in response to seismic cycles. Moving forward, resolution of uncertainty surrounding the relative timing of garnet growth in each setting (i.e., while attached to the slab or after incorporation in the mélange) may help to narrow these alternatives.

Putnis and John (2010) suggested that element incorporation may be principally influenced by the nature of transport properties rather than equilibrium partitioning. The observed elemental oscillations may therefore record transient and repeated episodes of rock-wide equilibration during prograde metamorphism, resulting from fluctuating element transport kinetics in grain boundaries that are decoupled from the advective fluid flow recorded by oxygen isotopes. Notably, equilibrated oscillations are present in highly partitioning, low concentration elements that have both rapid (i.e., Mn) and relatively slow (e.g., Y and HREE) lattice diffusivities. This may suggest that it is the effective concentration in the grain boundary rather than intragranular kinetic properties that control incorporation. Such changes could be driven by, for example, periodically changing grain boundary solubility.

It has been shown that modest temperature increases in eclogitic fluids may drive order-of-magnitude changes in element solubility (Tsay et al., 2017) meaning that more intense (100s of °C) transient heating (locally associated with, for example, intense mechanical heating during seismic slip) could lead to dramatic changes in garnet chemistry. Individual heating episodes may be localized and short-lived, but with sufficient regularity to be recorded widely over the timescales of garnet crystallization, leading to complex spatial overprinting of oscillatory 'events.' Such thermal spikes might also be expected to modify oxygen isotope partitioning between the fluid and garnet and thus drive associated changes in $\delta^{18}O$, but at the approximate ambient temperatures of garnet growth, this is expected to modify fractionation factors (from Vho et al., 2020) to a negligible degree. Extrinsic controls on reactive chemistry (and consequently, element uptake) as a viable mechanism for the incorporation of elemental oscillations remains a hypothesis for further investigation.

Conclusions

Observations in this study present a highly complex picture of element and oxygen isotope transfer at high pressure during subduction. The oscillatory elemental zoning that is so common in subduction zone garnet forms from an effective bulk composition that is equilibrated at the surface of garnet across the cm-scale, but cannot be simply linked to external fluid ingress that buffers the composition of the growing garnet.

The oxygen isotope zoning in garnet across the sample set is suggestive of significant spatiotemporal heterogeneity and episodicity in chemical transfer in subducting mafic lithologies, potentially inconsistent with a model of relatively homogeneous porous flow and associated buffering of the effective rock chemistry (e.g., Spandler et al., 2011). Evidence from the Oman rocks in this study, in addition to studies from other settings (e.g., Gerritts et al., 2019; Russel et al., 2013; Rubatto and Angiboust, 2014; Bovay et al., 2021), indicate that infiltration of external fluids can significantly modify the chemical, isotopic and redox state of the effective bulk composition, suggesting that high fluid–rock ratios can be locally achieved during subduction. However, evidence of such dramatic infiltration events was the exception among in the rocks of this study. Locally controlled and closed-system $\delta^{18}O$ records in garnet may represent the norm across a suite of representative samples. Consistent with the work of others (e.g., Zach and John et al., 2007; John et al., 2012; Angiboust & Raimondo, 2022), the developing picture of subduction is one in which blocks of subducting mafic crust generally maintain low permeability to sub-arc depths, with the majority of fluid transport occurring as, episodic high-flux events affecting discrete, volumetrically limited zones.

These findings highlight the importance of developing a deeper understanding of both the length scales across which elements equilibrate during garnet growth and the fundamental controls on elemental and isotopic mobility. It remains unclear what the driver of oscillatory elemental zoning may be, and how multiple potential drivers may produce a mixed oscillatory signature. Pulse-like changes in element solubility or efficiency of transport properties of the grain boundaries, decoupled from local pulses of fluid transfer and changes in isotopic composition of garnet, may require consideration.

Acknowledgments: The Smithsonian Institution's National Museum of Natural History is thanked for facilitating loans of samples from the Dominican Republic. Sampling in Greece, Oman and Venezuela was enabled by funding and/or field support from B.R. Hacker, E.M. Scott, H.A. Viete, Fulbright Australia and the Geological Society of London. G. Poirer and D. Dierkrup provided EPMA assistance at the University of Ottawa. FRG acknowledges financial support from the US–UK Fulbright Commission and Lloyd's of London in addition to a Blaustein Fellowship in the Department of Earth & Planetary Sciences, JHU. Microprobe work at the University of Ottawa and UCSB and SIMS work at the Australian National University was funded by JHU, UCSB and funds attached to the Blaustein Fellowship to FRG. Trace element raster mapping by LA–ICP–MS was supported by an NSF-EAR/IF grant (NSF-1831766) to DRV and MJH.

References

S. Angiboust, T. Raimondo, Permeability of subducted oceanic crust revealed by eclogite-facies vugs. *Geology*, *50*(8), 964-968 (2022).

S. Angiboust, T. Pettke, J. C. De Hoog, B. Caron, O. Oncken, Channelized fluid flow and eclogite-facies metasomatism along the subduction shear zone. *Journal of Petrology*, *55*(5), 883-916 (2014).

R. Anczkiewicz, J P. Platt, M. F. Thirlwall, J. Wakabayashi. Franciscan subduction off to a slow start: evidence from high-precision Lu–Hf garnet ages on high grade-blocks. *Earth and Planetary Science Letters*, *225*(1-2), 147-161 (2004)

L. P. Baumgartner, J. W. Valley, Stable isotope transport and contact metamorphic fluid flow. *Reviews in Mineralogy and Geochemistry*, *43*(1), 415-467 (2001).

G. E. Bebout, M. D. Barton, Fluid flow and metasomatism in a subduction zone hydrothermal system: Catalina Schist terrane, California. *Geology*, *17*(11), 976-980 (1989).

I. F. Blanco-Quintero, Y. Rojas-Agramonte, A. García-Casco, A. Kroner, D. F. Mertz, C. Lázaro, J. Blanco-Moreno, Timing of onset of subduction and rates of exhumation in a subduction channel: evidence from slab melts from La Corea mélange (eastern Cuba). In: Blanco-Quintero, I.F., Doctoral Thesis, pp. 59–91. (2010b)

I. F. Blanco-Quintero, A. García-Casco, T. V. Gerya, Tectonic blocks in serpentinite mélange (eastern Cuba) reveal large-scale convective flow of the subduction channel. *Geology*, *39*(1), 79-82 (2011).

T. Bovay, D. Rubatto, P. Lanari, Pervasive fluid-rock interaction in subducted oceanic crust revealed by oxygen isotope zoning in garnet. *Contributions to Mineralogy and Petrology*, *176*(7), 1-22 (2021).

C. M. Breeding, J. J. Ague, M. Bröcker, Fluid–metasedimentary rock interactions in subduction-zone mélange: implications for the chemical composition of arc magmas. *Geology*, *32*(12), 1041-1044 (2004).

A. Camacho, J. K. Lee, B. J. Hensen, J. Braun, Short-lived orogenic cycles and the eclogitization of cold crust by spasmodic hot fluids. *Nature*, *435*(7046), 1191-1196 (2005).

E. J. Chaves, S. Y. Schwartz, Monitoring transient changes within overpressured regions of subduction zones using ambient seismic noise. *Science Advances*, *2*(1), e1501289 (2016).

E. A. Codillo, V. Le Roux, H. R. Marschall, Arc-like magmas generated by mélange-peridotite interaction in the mantle wedge. *Nature Communications*, *9*(1), 1-11 (2018).

J. A. Connolly, Y. Y. Podladchikov, Fluid flow in compressive tectonic settings: Implications for midcrustal seismic reflectors and downward fluid migration. *Journal of Geophysical Research: Solid Earth*, *109*(B4) (2004).

A. M. Cruz-Uribe, F. Z. Page, E. Lozier, M. D. Feineman, T. Zack, R. Mertz-Kraus, D. E. Jacob, K. Kitajima, Trace element and isotopic zoning of garnetite veins in amphibolitized eclogite, Franciscan Complex, California, USA. *Contributions to Mineralogy and Petrology*, *176*(5), 1-19 (2021).

P. P. Dudley, Electron microprobe analyses of garnet in glaucophane schists and associated eclogites. *American Mineralogist: Journal of Earth and Planetary Materials*, *54*(7-8), 1139-1150 (1969)

J. E. Elkhoury, E. E. Brodsky, D. C. Agnew, Seismic waves increase permeability. *Nature*, *441*(7097), 1135-1138 (2006).

J. M. Garber, M. Rioux, M. P. Searle, A. R. Kylander-Clark, B. R. Hacker, J. D. Vervoort, A. J. Smye. Dating continental subduction beneath the Samail Ophiolite: garnet, zircon, and rutile petrochronology of the As Sifah eclogites, NE Oman. *Journal of Geophysical Research: Solid Earth*, *126*(12), e2021JB022715 (2021).

A. García-Casco, R. L. Torres-Roldán, G. Millán, P. Monié, J. Schneider, Oscillatory zoning in eclogitic garnet and amphibole, Northern Serpentinite Melange, Cuba: a record of tectonic instability during subduction? *Journal of Metamorphic Geology*, *20*(6), 581-598 (2002).

A. R. Gerrits, E. C. Inglis, B. Dragovic, P. G. Starr, E. F. Baxter, K. W. Burton, Release of oxidizing fluids in subduction zones recorded by iron isotope zonation in garnet. *Nature Geoscience*, *12*(12), 1029-1033 (2019).

P. Herms, T. John, R. J. Bakker, V. Schenk, Evidence for channelized external fluid flow and element transfer in subducting slabs (Raspas Complex, Ecuador). *Chemical Geology*, *310*, 79-96 (2012).

D. D. Hickmott, S. S. Sorensen, P. S. Z. Rogers, Metasomatism in a subduction complex: Constraints from microanalysis of trace elements in minerals from garnet amphibolite from the Catalina Schist. *Geology*, *20*(4), 347-350 (1992).

F. Higashino, D. Rubatto, T. Kawakami, A. S. Bouvier, L. P. Baumgartner, Oxygen isotope speedometry in granulite facies garnet recording fluid/melt–rock interaction (Sør Rondane Mountains, East Antarctica). *Journal of Metamorphic Geology*, *37*(7), 1037-1048 (2019).

M. B. Holness, Temperature and pressure dependence of quartz-aqueous fluid dihedral angles: the control of adsorbed H_2O on the permeability of quartzites. *Earth and Planetary Science Letters*, *117*(3-4), 363-377 (1993).

T. Hyppolito, A. Cambeses, S. Angiboust, T. Raimondo, A. García-Casco, C. Juliani, Rehydration of eclogites and garnet-replacement processes during exhumation in the amphibolite facies. *Geological Society, London, Special Publications*, *478*(1), 217-239 (2019).

B. Jamtveit, K. V. Ragnarsdottir, B. J. Wood, On the origin of zoned grossular-andradite garnets in hydrothermal systems. *European Journal of Mineralogy*, *7*(6), 1399-1410 (1995).

T. John, N. Gussone, Y. Y. Podladchikov, G. E. Bebout, R. Dohmen, R. Halama, T. Magna, H. M. Seitz, Volcanic arcs fed by rapid pulsed fluid flow through subducting slabs. *Nature Geoscience*, *5*(7), 489-492 (2012).

M. F. Kabir, A. Takasu, Evidence for multiple burial–partial exhumation cycles from the Onodani eclogites in the Sambagawa metamorphic belt, central Shikoku, Japan. *Journal of Metamorphic Geology*, *28*(8), 873-893 (2010).

R. Kessel, T. Pettke, P. Fumagalli, Melting of metasomatized peridotite at 4–6 GPa and up to 1200 °C: an experimental approach. *Contributions to Mineralogy and Petrology*, *169*(4), 37 (2015).

M. J. Kohn, J. W. Valley, D. Elsenheimer, M. J. Spicuzza, O isotope zoning in garnet and staurolite: evidence for closed-system mineral growth during regional metamorphism. *American Mineralogist*, *78*(9-10), 988-1001 (1993).

T. Kogiso, Y. Tatsumi, S. Nakano, Trace element transport during dehydration processes in the subducted oceanic crust: 1. Experiments and implications for the origin of ocean island basalts. *Earth and Planetary Science Letters*, *148*(1-2), 193-205 (1997).

M. Konrad-Schmolke, T. Zack, P. J. O'Brien, D. E. Jacob, Combined thermodynamic and rare earth element modelling of garnet growth during subduction: examples from ultrahigh-pressure eclogite of the Western Gneiss Region, Norway. *Earth and Planetary Science Letters*, *272*(1-2), 488-498 (2008).

M. Konrad-Schmolke, R. Halama, R. Wirth, A. Thomen, N. Klitscher, L. Morales, A. Schreiber, F. D. Wilke, Mineral dissolution and reprecipitation mediated by an amorphous phase. *Nature Communications*, *9*(1), 1-9 (2018).

Lagos, M., Scherer, E. E., Tomaschek, F., Münker, C., Keiter, M., Berndt, J., & Ballhaus, C. (2007). High precision Lu–Hf geochronology of Eocene eclogite-facies rocks from Syros, Cyclades, Greece. *Chemical Geology*, *243*(1-2), 16-35.

J. L. Li, R. Klemd, J. Gao, T. John, Poly-cyclic metamorphic evolution of eclogite: evidence for multistage burial–exhumation cycling in a subduction channel. *Journal of Petrology*, *57*(1), 119-146 (2016).

N. S. Mancktelow, G. Pennacchioni, The influence of grain boundary fluids on the microstructure of quartz-feldspar mylonites. *Journal of Structural Geology*, *26*(1), 47-69 (2004).

L. A. Martin, D. Rubatto, C. Crépisson, J. Hermann, B. Putlitz, A. Vitale-Brovarone, Garnet oxygen analysis by SHRIMP-SI: Matrix corrections and application to high-pressure metasomatic rocks from Alpine Corsica. *Chemical Geology*, *374*, 25-36 (2014).

D. B. Meier, H. N. Waber, T. Gimmi, F. Eichinger, L. W. Diamond, Reconstruction of in-situ porosity and porewater compositions of low-permeability crystalline rocks: Magnitude of artefacts induced by drilling and sample recovery. *Journal of Contaminant Hydrology*, *183*, 55-71 (2015).

K. Mibe, T. Yoshino, S. Ono, A. Yasuda, T. Fujii, Connectivity of aqueous fluid in eclogite and its implications for fluid migration in the Earth's interior. *Journal of Geophysical Research: Solid Earth*, *108*(B6) (2003).

F. Z. Page, E. J. Essene, S. B. Mukasa, J. W. Valley, A garnet–zircon oxygen isotope record of subduction and exhumation fluids from the Franciscan Complex, California. *Journal of Petrology*, *55*(1), 103-131 (2014).

S. C. Penniston-Dorland, L. P. Baumgartner, B. Dragovic, A. S. Bouvier, Li isotope zoning in garnet from Franciscan eclogite and amphibolite: The role of subduction-related fluids. *Geochimica et Cosmochimica Acta*, *286*, 198-213 (2020).

F. Piccoli, J. J. Ague, X. Chu, M. Tian, A. Vitale Brovarone, Field-based evidence for intra-slab high-permeability channel formation at eclogite-facies conditions during subduction. *Geochemistry, Geophysics, Geosystems*, *22*(3), e2020GC009520 (2021).

A. Putnis, T. John, Replacement processes in the Earth's crust. *Elements*, *6*(3), 159-164 (2010).

O. Plümper, T. John, Y. Y. Podladchikov, J. C. Vrijmoed, M. Scambelluri, Fluid escape from subduction zones controlled by channel-forming reactive porosity. *Nature Geoscience*, *10*(2), 150-156 (2017).

A. K. Russell, K. Kitajima, A. Strickland, L. G. Medaris, D. J. Schulze, J. W. Valley, Eclogite-facies fluid infiltration: constraints from δ 18 O zoning in garnet. *Contributions to Mineralogy and Petrology*, *165*(1), 103-116 (2013).

D. Rubatto, S. Angiboust, Oxygen isotope record of oceanic and high-pressure metasomatism: a P–T–time–fluid path for the Monviso eclogites (Italy). *Contributions to Mineralogy and Petrology*, *170*(5), 1-16 (2015).

M. W. Schmidt, S. Poli, Experimentally based water budgets for dehydrating slabs and consequences for arc magma generation. *Earth and Planetary Science Letters*, *163*(1-4), 361-379 (1998).

R. Schumacher, K. Rötzler, W. V. Maresch, Subtle oscillatory zoning in garnet from regional metamorphic phyllites and mica schists, western Erzgebirge, Germany. *The Canadian Mineralogist*, *37*(2), 381-403 (1999).

M. R. Scicchitano, M. J. Spicuzza, E. T. Ellison, D. Tuschel, A. S. Templeton, J. W. Valley, In Situ Oxygen Isotope Determination in Serpentine Minerals by SIMS: Addressing Matrix Effects and Providing New Insights on Serpentinisation at Hole BA1B (Samail ophiolite, Oman). *Geostandards and Geoanalytical Research*, *45*(1), 161-187 (2021).

A. J. Smye, C. J. Warren, M. J. Bickle, The signature of devolatisation: extraneous 40Ar systematics in high-pressure metamorphic rocks. *Geochimica et Cosmochimica Acta*, *113*, 94-112 (2013).

C. Spandler, T. Pettke, D. Rubatto, Internal and external fluid sources for eclogite-facies veins in the Monviso meta-ophiolite, Western Alps: implications for fluid flow in subduction zones. *Journal of Petrology*, *52*(6), 1207-1236 (2011).

H. Staudigel, T. Plank, T. B. White, H. U. Schmincke, Geochemical fluxes during seafloor alteration of the basaltic upper oceanic crust: DSDP Sites 417 and 418. *Subduction: Top to Bottom*, *96*, 19-38 (1996).

H. H. Stowell, T. Menard, C. K. Ridgway, Ca-metasomatism and chemical zonation of garnet in contact-metamorphic aureoles, Juneau Gold Belt, southeastern Alaska. *The Canadian Mineralogist*, *34*(6), 1195-1209 (1996).

S. Taetz, T. John, M. Bröcker, C. Spandler, A. Stracke, Fast intraslab fluid-flow events linked to pulses of high pore fluid pressure at the subducted plate interface. *Earth and Planetary Science Letters*, *482*, 33-43 (2018).

Z. Tan, P. Agard, J. Gao, T. Hong, B. Wan, Concordant pulse in Mn, Y and HREEs concentrations during UHP eclogitic garnet growth: transient rock dynamics along a cold subduction plate interface. *Earth and Planetary Science Letters*, *530*, 115908 (2020).

L. Tajčmanová, Y. Podladchikov, R. Powell, E. Moulas, J. C. Vrijmoed, J. A. D. Connolly, Grain-scale pressure variations and chemical equilibrium in high-grade metamorphic rocks. *Journal of Metamorphic Geology*, *32*(2), 195-207 (2014).

R. Tamblyn, M. Hand, D. Kelsey, R. Anczkiewicz, D. Och, Subduction and accumulation of lawsonite eclogite and garnet blueschist in eastern Australia. *Journal of Metamorphic Geology*, *38*(2), 157-182 (2020).

A. Tsay, Z. Zajacz, P. Ulmer, C. Sanchez-Valle, Mobility of major and trace elements in the eclogite-fluid system and element fluxes upon slab dehydration. *Geochimica et Cosmochimica Acta*, *198*, 70-91 (2017).

J. B. Walters, A. M. Cruz-Uribe, W. J. Song, C. Gerbi, K. Biela, Strengths and limitations of in situ U-Pb titanite petrochronology in polymetamorphic rocks: An example from western Maine, USA (2021).

C. J. Warren, S. C. Sherlock, S. P. Kelley, Interpreting high-pressure phengite 40 Ar/39 Ar laserprobe ages: an example from Saih Hatat, NE Oman. *Contributions to Mineralogy and Petrology*, *161*(6), 991-1009 (2011).

D. J. Van Hinsbergen, M. Maffione, L. M. Koornneef, C. Guilmette, Kinematic and paleomagnetic restoration of the Semail ophiolite (Oman) reveals subduction initiation along an ancient Neotethyan fracture zone. *Earth and Planetary Science Letters*, *518*, 183-196 (2019).

A. Vho, P. Lanari, D. Rubatto, An internally-consistent database for oxygen isotope fractionation between minerals. *Journal ofPpetrology*, *60*(11), 2101-2129 (2019).

A. Vho, P. Lanari, D. Rubatto, J. Hermann, Tracing fluid transfers in subduction zones: an integrated thermodynamic and $\delta^{18}O$ fractionation modelling approach. *Solid Earth*, *11*(2), 307-328 (2020).

Viete, D. R., Kylander-Clark, A. R., & Hacker, B. R. (2015). Single-shot laser ablation split stream (SS-LASS) petrochronology deciphers multiple, short-duration metamorphic events. *Chemical Geology*, *415*, 70-86.

D. R. Viete, B. R. Hacker, M. B. Allen, G. G. Seward, M. J. Tobin, C. S. Kelley, G. Cinque, A. R. Duckworth, Metamorphic records of multiple seismic cycles during subduction. *Science Advances*, *4*(3), eaaq0234 (2018).

B. W. D. Yardley, C. A. Rochelle, A. C. Barnicoat, G. E. Lloyd, Oscillatory zoning in metamorphic minerals: an indicator of infiltration metasomatism. *Mineralogical Magazine*, *55*(380), 357-365 (1991).

T. Zack, T. John, An evaluation of reactive fluid flow and trace element mobility in subducting slabs. *Chemical Geology*, *239*(3-4), 199-216 (2007).

FIGURES AND TABLES

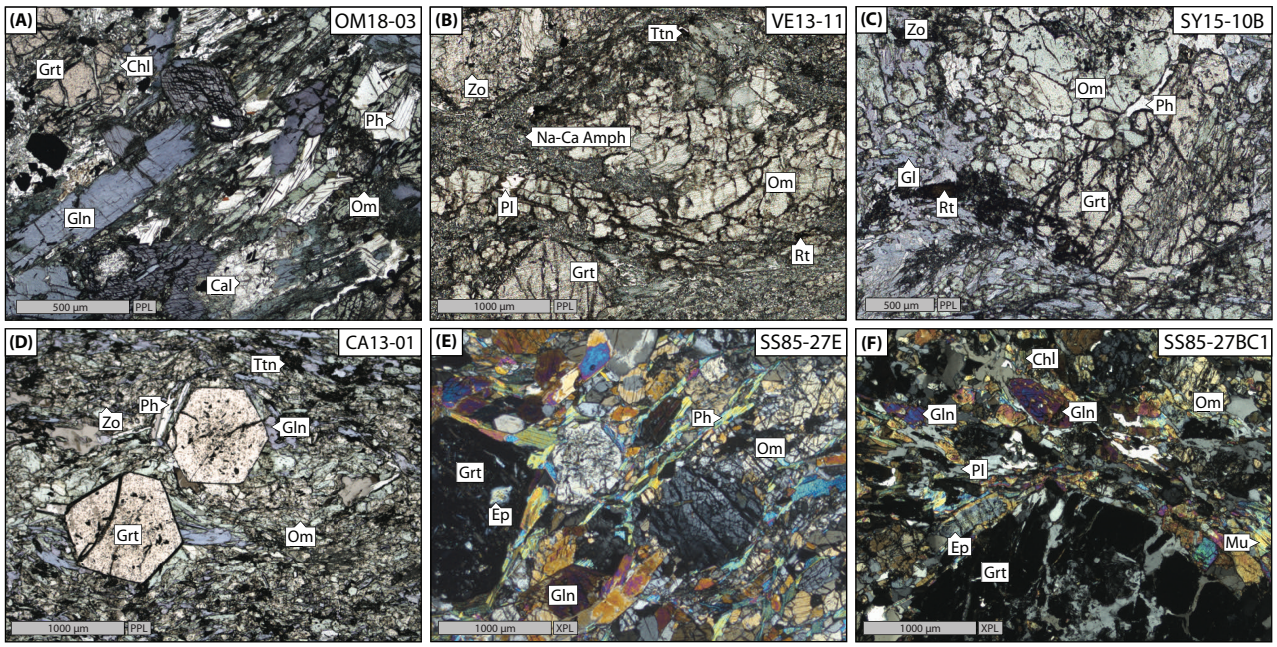

Figure 1. Representative thin section photomicrographs of select samples. (**A**) Plane-polarized photomicrograph of retrogressed eclogite OM18-03C from As Sifah, Oman. (**B**) Plane-polarized photomicrograph of foliated amphibolite–eclogite VE13-11 from Puerto Cabello, Venezuela. (**C**) Plane-polarized photomicrograph of coarse blueschist–eclogite SY15-10B from Syros, Greece. (**D**) Plane-polarized photomicrograph of foliated blueschist–eclogite CA13-01 from Ring Mountain, California. (**E**) Cross-polarized photomicrograph of core eclogite SS85-27A from Punta Balandra, Dominican Republic. (**F**) Cross-polarized photomicrograph of altered rind eclogite SS85-27BC1 from Punta Balandra, Dominican Republic.

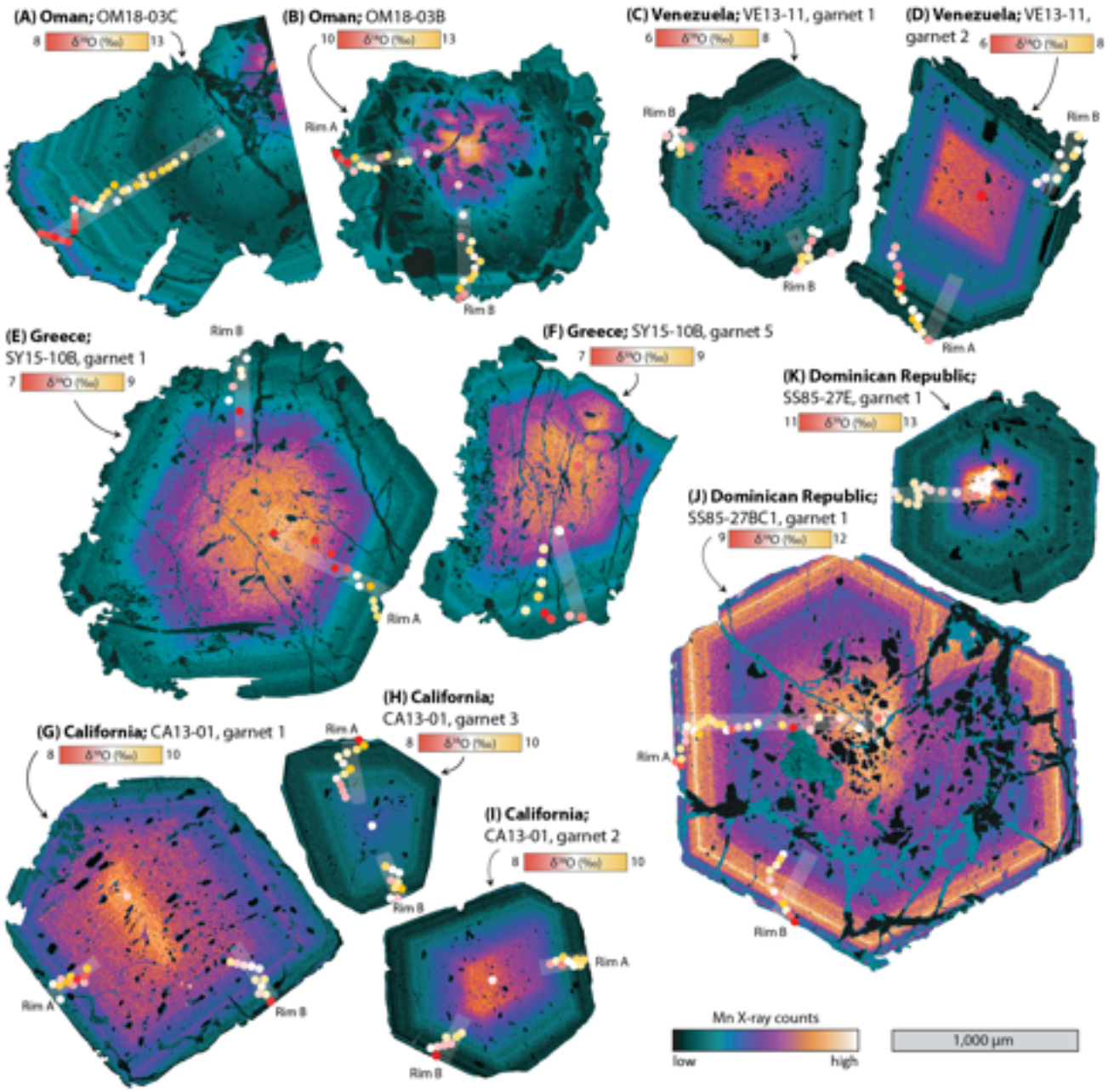

Figure 2. X-ray count maps of Mn zoning, and locations and O-isotope compositions for analyzed garnets from a suite of exhumed *HP–LT* subduction zones. (**A**) and (**B**) Garnets from samples collected meters apart in outcrop from As Sifah, Oman; (**C**) and (**D**) two garnets from the same thin section from Puerto Cabello, Venezuela; (**E**) and (**F**) two garnets from the same thin section from Syros, Greece; (**G**), (**H**) and (**I**) garnets from one thin section from Ring Mountain, California; (**J**) and (**K**) eclogite rind and core garnets, respectively, from Punta Balandra, Dominican Republic. X-ray maps show relative counts in garnets (matrix regions have been masked but inclusions in garnet are preserved) and are scaled to a single length scale. Spots give location and SIMS points (scaled 2x actual size) and are colored according to their $\delta^{18}O$ value using color scales specific to each grain.

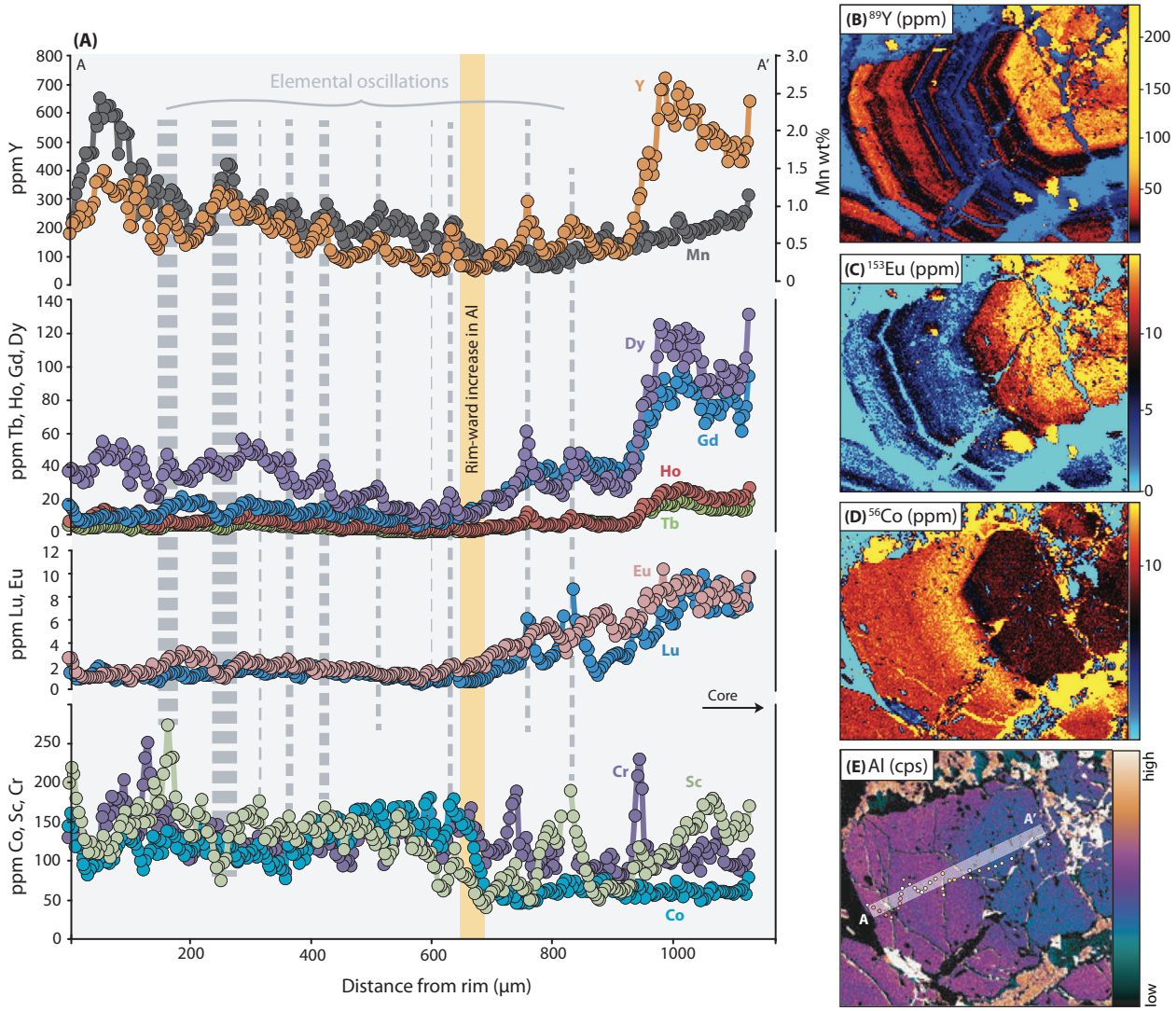

793

794 **Figure 3. Trace elements and Al zoning in garnet 1 from sample OM18-03C.** (**A**) LA–ICP–MS trace
795 element profile along transect in Fig. 1A. (**B**), (**C**), and (**D**) LA–ICP–MS maps of Y, Eu and Co zoning,
796 respectively. (**E**) X-ray map of Al content, showing position of profile in (**A**) and of SIMS points.

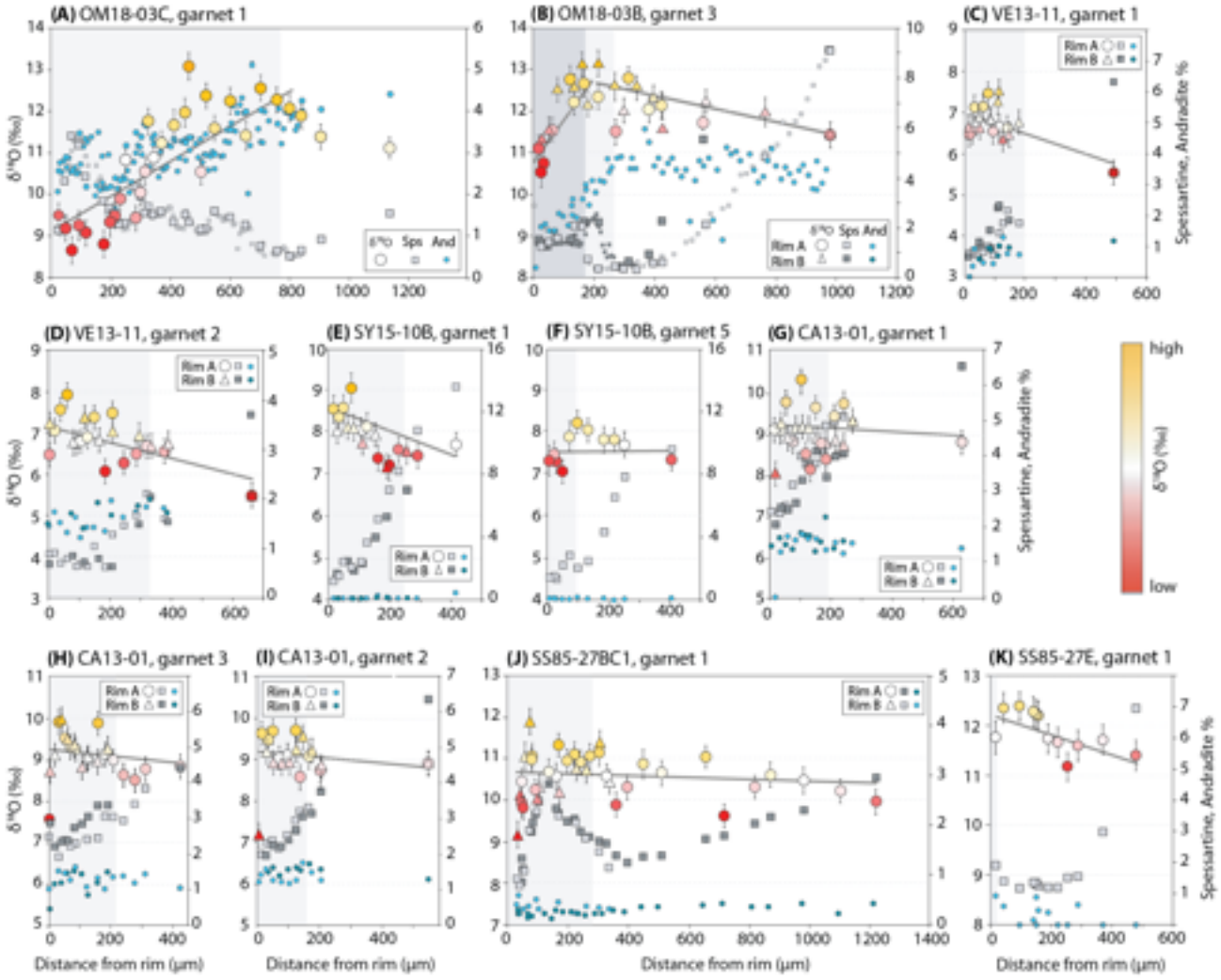

Figure 4. Oxygen isotope and elemental zoning across garnet plotted with distance from external rim. **(A)**–**(K)** lettering scheme as for Fig. 1. $\delta^{18}O$ values for a given grain across opposing rims are plotted on a single scale as large circles and triangles to highlight asymmetry in $\delta^{18}O$ zoning across garnet cores. $\delta^{18}O$ points are colored as in Fig. 2, and error bars represent ± 1σ uncertainty obtained by propagation of the internal error, the error on mass fractionation correction, and the error on the matrix effect correction. Squares show spessartine content used for matrix correction (small gray squares in (A) and (B) are high-sampling resolution profiles across same transect). Small blue circles show calculated andradite content. On all plots, gray shaded region denotes the region of persistent oscillatory zoning in Mn from Fig. 2.

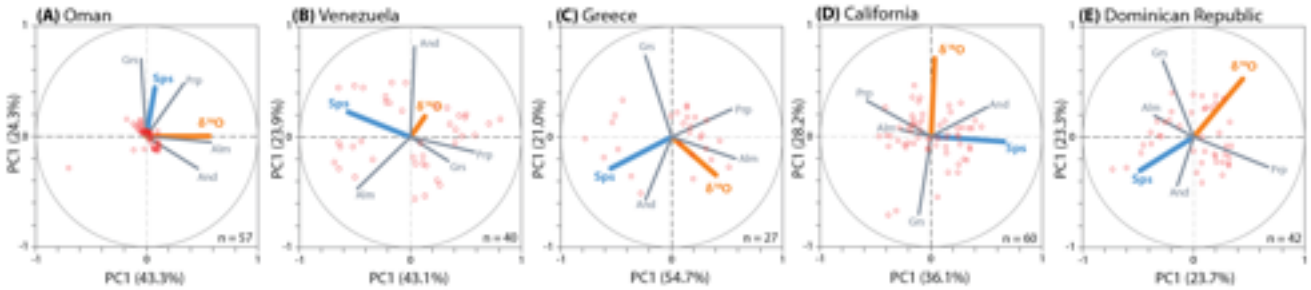

Figure 5. Results of principal component analyses. (A)–(E) Log-transformed and scaled coordinate values for PC1 versus. PC2 loadings, and corresponding scores and eigenvectors for data from all garnets assessed with SIMS. The number of analyses included in each PCA are shown, and the percentage on each axis represents the total variance explained by that component.

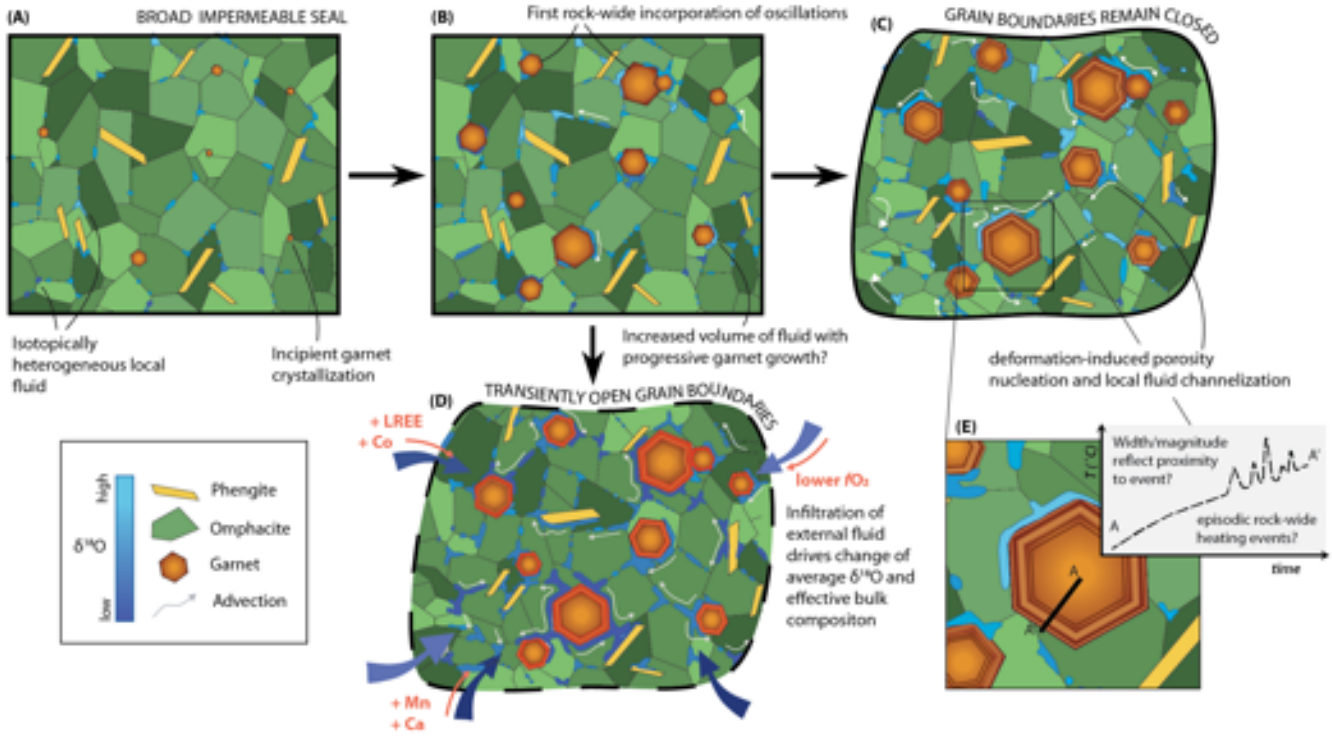

Figure 6. Conceptual model for the migration of grain boundary fluid during garnet growth in low-porosity *HP–LT* metabasites. (**A**)–(**C**) Typical rock-wide evolution with non-interconnected and isotopically heterogenous fluid, involving local porosity nucleation, micro-channelization, and fluid migration. (**D**) Less common scenario in which grain boundaries are transiently opened, permitting ingress of external, chemically and isotopically distinct, fluids that buffer a change in the stable mineral (i.e., garnet) composition (**E**) Hypothesized heating scenario versus time that may account for changing elemental solubility at the surface of grains and episodic equilibration, decoupled from fluid infiltration (or lack thereof) events.

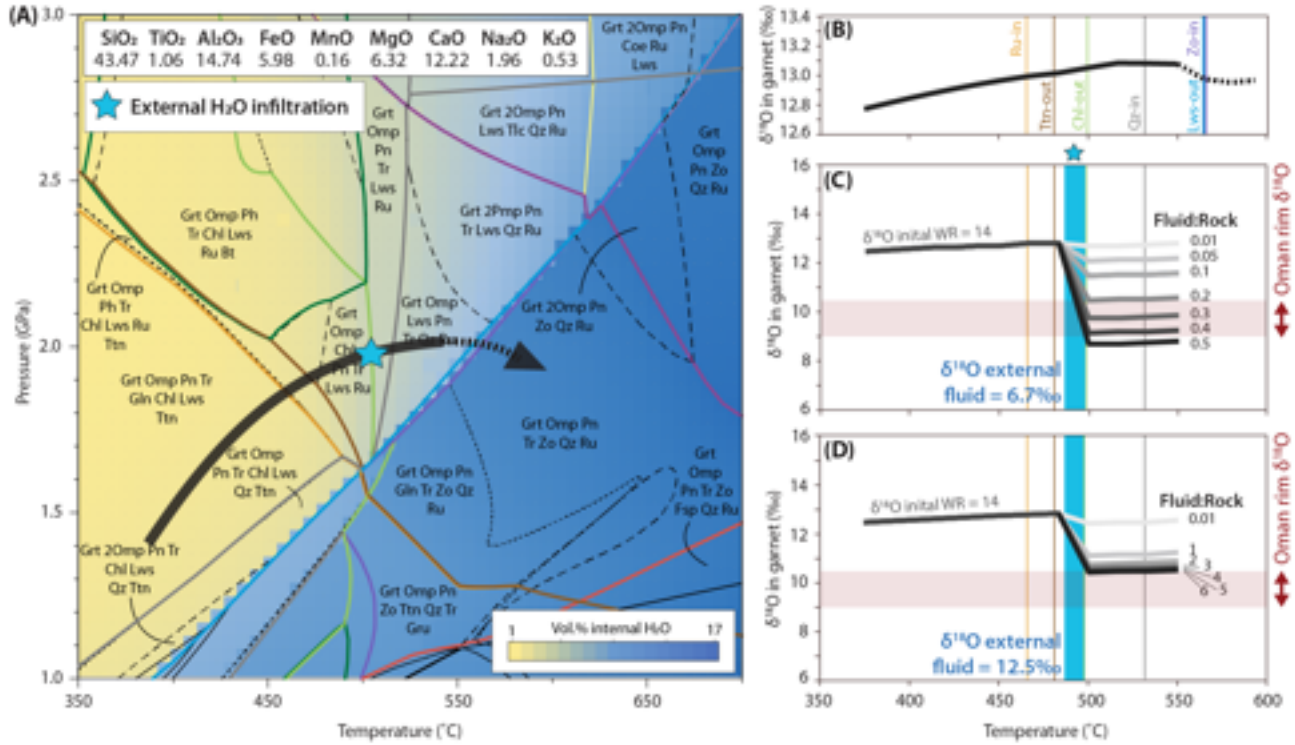

Figure 7. Results of phase equilibria and fluid–rock interaction modelling. (**A**) Phase equilibria for average altered metabasalt of Staudigel et al. (1996). Pressure–temperature path and peak metamorphic conditions of Oman eclogite evolution adopted from Warren and Waters (2001) and Searle et al. (1994). Blue star represents position/timing of simulated fluid ingress, short, dashed line shows additional *P–T* evolution required to dehydrate lawsonite. Mineral abbreviations after Whitney and Evans (2010). (**B**) Modelled $\delta^{18}O$ in garnet versus temperature along the full (including dashed) prograde path in (**A**), with no external fluid infiltration. (**C**) Modelled $\delta^{18}O$ in garnet versus temperature along solid line in (**A**) for infiltration of serpentinite-derived fluid with $\delta^{18}O = 6.7\%$. (**D**) As in (**C**) but for sediment-derived fluid with $\delta^{18}O = 12.5\%$.

TABLES

Locality	Coordinates	Sample reference	HP (+ secondary) assemblage	Peak temperature (°C)	Peak pressures (GPa)	Approx. age of (peak) metamorphism
Oman	23.43942°N, 058.76980°E	OM18-03B	Grt, Omp, Gln, Ph, Rt, Qz (Act, Ab, Chl, Cal, Py)	40–520	1.8–2.0	81–77 Ma[a]
		OM18-03C				
Venezuela	10.46530°N, 067.94255°W	VE13-11	Grt, Omp, Amp, Zo, Rt, Qz (Ab, Amp, Chl)	(A) 550–600 (B) 450–520	(A) 1.6–1.8 (B) 1.8	28–42 Ma[b]
Greece	37.50175°N, 024.92664°E	SY15-10	Grt, Gln, Omp, Ph, Alb, Rt, Zo, Lws (Chl, Ttn, Amph)	550	1.4–1.8	52–50 Ma[c]
California	37.91788°N, 122.49305°W	CA13-01	Grt, Omp, Gln, Zo, Qz, Rt (Chl, Ttn)	555–585	1.4–1.95	157–158 Ma[d]
Dominican Republic	19.18206°N, 069.23367°W	SS85-27E	Grt, Omp, Ph, Gln, Ep, Rt, Ttn, Qz (Chl, Hem)	(A) 450 ± 70 (B) 550–625	(A) 1.3 ± 0.2 (B) 2–2.4	115–110 Ma[e]
	19.18206°N, 069.23367°W	SS85-27BC1	Grt, Omp, Ph, Gln (Act, Ab, Chl)			

Table 1. Summary of samples used in this study. Mineral abbreviations after Whitney and Evans (2010). [a] Garber et al., 2021. [b] Viete et al., 2015. [c] Lagos et al., 2007. [d] Anczkiewicz et al., 2004. [e] Blanco-Quintero et al., 2010b.

Sample	Grain	Spessartine + $\delta^{18}O$					ΔSpessartine + $\Delta\delta^{18}O$				
		N	CoVar	r-value	P	95%	N	CoVar	r-value	P	95%
OM18-03C	g1	30	-0.01	-0.68	$5x10^{-5}$	sig.	29	0.00	-0.30	0.22	not sig.
OM18-03B	g3	28	0.00	-0.24	0.23	not sig.	26	0.00	-0.25	0.22	not sig.
VE13-11	g1	18	0.00	0.21	0.40	not sig.	17	0.01	0.43	0.08	not sig.
VE13-11	g2	22	0.00	-0.28	0.20	not sig.	20	0.00	0.39	0.09	not sig.
CA13-01	g3	17	-0.00	-0.01	0.97	not sig.	16	0.00	-0.09	0.87	not sig.
CA13-01	g2	22	0.00	0.16	0.47	not sig.	21	0.00	0.23	0.45	not sig.
CA13-01	g1	21	0.00	-0.38	0.09	not sig.	19	0.00	-0.27	0.31	not sig.
SS85-27BC1	g1	37	-0.00	-0.11	0.55	not sig.	35	0.00	0.02	0.92	not sig.
SS85-27E	g1	13	-0.00	-0.45	0.12	not sig.	12	-0.00	-0.29	0.36	not sig.
SY15-10B	g5	10	0.00	0.32	0.38	not sig.	9	0.00	-0.25	0.51	not sig.
SY15-10B	g1	17	-0.02	-0.77	$3x10^{-4}$	sig.	16	0.00	-0.16	-0.56	not sig.

Table 2. Covariance and correlation between $\delta^{18}O$ and corresponding spessartine content at the 95% confidence level for garnets in Fig. 1 and 2. Results for both raw recalculated analyses and for the difference (Δ) between adjacent analyses.

SUPPLEMENTARY MATERIAL 1

Sample descriptions and conditions of metamorphism

OM18-03 – Omani samples OM18-03B and OM18-03C were collected from As Sifah (23.43942°N, 058.76980°E), very close to the AS-85 'vein' locality of El Shazly et al. (1997) The high-pressure matrix assemblage contains omphacite, glaucophane, phengite, rutile, quartz, and garnet, and is overprinted by foliation-parallel actinolite and plagioclase symplectites, and clots containing chlorite, calcite, pyrite, and actinolite (Fig. 7A). Glaucophane is strongly zoned with dark barroisite rims. Anhedral garnet is replaced by chlorite and green amphibole along an irregular fracture network and contains abundant aligned inclusions of rutile, epidote and quartz. Using mineral compositions obtained in this study, the garnet–phengite–omphacite barometer of Waters et el. (1993) and garnet–pyroxene thermometer of Ravna (2000) indicate peak pressures of 1.8–2.0 GPa and temperatures of 490–520 °C, respectively. Peak *P–T* conditions have been interpreted to have been attained along relatively cool, clockwise *P–T* path, prior to near-isothermal decompression (El Shazly et al., 1990) and pervasive greenschist facies overprinting.

VE13-11 – Venezuelan sample VE13-11, is an eclogite amphibolite from the Nirgua Complex of the Cordillera de la Costa, collected near to Puerto Cabello (10.46530°N, 067.94255°W). It comprises millimeter-sized garnets wrapped by a retrogressed matrix that contains clots and bands of omphacite (Fig. 7B), which have been amphibolitized to symplectites of calcic amphibole and albite. Ca–Na amphiboles with a compositional array between actinolite and intermediate barroisite approximately define the matrix foliation. Minor glaucophane, calcite and Fe-oxides are present, and matrix titanite contains cores of rutile. Subhedral garnet porphyroblasts contain inclusions of omphacite, zoisite, glaucophane, Na–Ca amphibole, rutile, and very rare quartz and albite. Phase equilibria modelling as part of this study constrains the peak eclogite amphibolite facies assemblage to 1.6–1.8 GPa and 550–600 °C, higher than results of conventional thermobarometry (~1.8 GPa and 450–520 °C; Sisson et al., 1997). A clockwise prograde evolution has been discerned from associated eclogitic blocks from the Nirgua Complex of the Cordillera de la Costa (Sisson et al., 1997).

SY15-10 – Greek sample SY15-10, an intermixed garnet blueschist–eclogite, was collected from the Cycladic Blueschist Unit at Grizzas Bay, Syros (37.50175°N, 024.92664°E). The variably foliated matrix contains glaucophane, omphacite, phengite, albite, rutile rimmed by titanite, coarse titanite, zoisite, and rare lawsonite (Fig. 7C). Clots of late chlorite and amphibole are also present. Coarse (≤ 3 mm) glaucophane plates contain inclusions of omphacite, garnet, and phengite. 0.7–1.5 mm-diameter garnets are relatively scarce, and their cores contain inclusions of phengite, glaucophane and rutile. Thermobarometric estimates suggest blueschists and eclogites of Syros experienced near-isothermal decompression after reaching 1.4–1.8 GPa and ~550 °C along a clockwise *P–T* path (Trotet et al., 2001; Putlitz et al., 2005). No pseudomorphs of lawsonite were found preserved in garnet from this sample, but lawsonite-bearing assemblages have been extensively documented across the island of Syros (e.g., Putlitz et al., 2005), and imply that the *P–T* conditions never far exceeded the stability field of lawsonite.

CA13-01 – Californian sample CA13-01 has been described in detail in Viete et al. (2018). It is a strongly foliated and interlayered blueschist–eclogite containing garnet porphyroblasts 0.5–2 mm in diameter, originating from a Ring Mountain *HP–LT* block (37.91788°N, 122.49305°W). The matrix contains

omphacite, glaucophane, zoisite, quartz, and rutile. In addition to retrograde matrix chlorite, rutile is partially replaced by titanite (Fig. 7D). Phase equilibria modelling of Viete et al. (2018) constrained peak metamorphic conditions of this sample to 1.4–1.95 GPa and 555–585°C, after a counterclockwise prograde *P–T* path and prior to refrigeration and exhumation (Tsujimori et al., 2006).

SS85-27 – Dominican samples SS85-27E and SS85-27BC1 were collected by Sorena Sorensen (obtained from the Smithsonian Institution collection) from a polished beach outcrop at Punta Balandra, Dominican Republic (19.18206°N, 069.23367°W), and have been interpreted to represent the core and rind, respectively, of an interlayered blueschist–eclogite mélange block (Catlos & Sorensen, 2003). Core sample SS85-27E comprises a moderately foliated matrix of omphacite, phengite, glaucophane, epidote, rutile, titanite, and subhedral to euhedral, 0.5–2 mm garnet porphyroblasts (Fig. 7E). Minor quartz, and retrograde chlorite and hematite is also present. Rind sample SS85-27BC1 contains coarse garnets (0.5–3 mm diameter) in a similarly foliated matrix of epidote, omphacite, phengite and glaucophane, with late actinolite and albite (Fig. 7F). Matrix titanite contains rutile cores. Garnet is extensively chloritized along cracks, and inclusion rich cores (that are often partially atollized in the rind) contain quartz, epidote, phengite, and epidote and paragonite that are interpreted to represent pseudomorphs after lawsonite. Minimum *P–T* conditions achieved by associated Punta Balandra blocks were constrained to 1.3 ± 0.2 GPa and 450 ± 70 °C (Goncalves et al., 2000), although Escuder-Viruete and Pérez-Estaún (2006) discerned a clockwise prograde evolution from lawsonite-blueschist facies to peak phengite-eclogite facies conditions at 2.2–2.4 GPa and 550–625 °C.

SUPPLEMENTARY MATERIAL 2

Analytical Approaches & Methodologies

Elemental characterization using electron probe and laser ablation mass spectrometry

For samples from California, Greece, Oman and Venezuela, EPMA mapping of garnet porphyroblasts was performed using a Cameca SX100 at the Department of Earth Science, University of California, Santa Barbara. X-ray maps were collected using a 15 kV accelerating voltage, 200 nA current and dwell time of 50 ms (100 ms for CA13-01). Garnets from the Dominican Republic were mapped in the Department of Earth Science, University of Ottawa, using a JEOL 8230 Superprobe. Analytical conditions were 20 kV and 400 nA, with a dwell time of 100 ms. In both routines, wavelength dispersive spectroscopy (WDS) measured Fe, Mg, Ca, Mn, and Al in a single pass; quantitative maps were obtained via a Si-by-difference and O-stoichiometry approach, with a mean atomic number background correction. Mapping used a square grid with spatial resolution 3–6 μm, depending on grain size. Calculation of the andradite component in garnet from EPMA analyses was carried out using the charge-balance method described by Quinn et al. (2016).

LA–ICP–MS mapping was conducted on garnet from Oman in the Department of Earth & Planetary Sciences, Johns Hopkins University. Analyses were performed using a Teledyne Cetac Analyte G2 193 nm excimer LA system with a Helex II two-volume ablation cell coupled to an Agilent 8900 triple quadrupole ICP-MS via 1 mm PEEK tubing. Parallel LA raster line scans used a 10 μm x 10 μm square laser aperture, a 100 Hz repetition rate, and a fluence of 1.5 J/cm^2. Scan speeds of 26 μm/s were chosen to

synchronize the pulse frequency and ICP-MS acquisition time and minimize aliasing. Ablation was performed in a He carrier gas (0.575 mL min^{-1}) mixed downstream with Ar (1.3 L min^{-1}). Each line scan was followed by 10 s of washout. Integrated line scans were generated offline using the internally standardized 'Trace Element' reduction scheme included in Iolite4 (Hellstrom et al., 2008; Paton et al., 2011). Quantification of laser data was completed using the measured (by EPMA) average value of Si in garnet and an internal NIST612 standard reference material. Periodic raster linescans along NIST610 were used as an additional check on data quality.

***In situ* oxygen isotope analysis**

In situ oxygen isotopes were measured in 11 garnets from across six samples using the SHRIMP–SI instrument at the Research School of Earth Sciences, Australian National University (ANU). Measurements were made over two analytical sessions (September 2017 and August 2020). SHRIMP-SI measurements were performed with a 15 kV Cs^+ primary ion beam with a current of ~2 nA producing an elliptical spot measuring 25 x 20 µm. Charge neutralization at the surface was achieved by a focused electron beam with an energy of ~1.9 keV. Secondary $^{16}O^-$ and $^{18}O^-$ ion signals were collected simultaneously in Faraday cups and ion currents measured on iFlex electrometers set to 10^{11} Ω (Ávila et al., 2020). Each spot measurement took 6 min and consisted of a single set of six subsets (20 s measurement each) with each comprising ten 2 s integrations. Background and electron induced secondary ion emission (EISIE) counts were subtracted from all the data presented here. Isotopic ratios ($^{18}O/^{16}O$) are reported in delta notation ($\delta^{18}O$) relative to Vienna Standard Mean Ocean Water (VSMOW; Baertschi, 1976). Analyses of unknown garnets were bracketed by measurement of UWG-2 garnet ($\delta^{18}O$ = +5.8‰; Valley et al., 1995) which was used as the primary reference material and to monitor instrument stability and measurement repeatability.

The garnet matrix-effect correction scheme follows the protocol described by Martin et al. (2014). Reference materials were measured during September 2017 and August 2020 SHRIMP–SI sessions. Instrumental bias as a function of grossular and spessartine components were calculated from the data obtained during the 2017 and 2020 sessions as well as data acquired in previous calibrations using the SHRIMP-SI instrument at ANU (Martin et al., 2014). The calculated bias correction due to the grossular and spessartine components are given by the equations:

$$Bias_{Gr} = -10.06X^2_{Gr} + 12.77X_{Gr} - 1.467$$
$$Bias_{Spe} = -4.31X^2_{Spe} + 6.91X_{Spe} - 0.07.$$

The precision on the matrix effect correction, calculated as residuals on the grossular and spessartine calibration curves, are σ_{Gr} = 0.34‰ and σ_{And} = 0.28‰ (2σ). The internal error on individual oxygen isotopic analyses ranges 0.06–0.23‰ (2σ). The reported single spot uncertainty ("external error") was calculated using the within-spot precision ("internal error"), the precision on the matrix effect, and the repeatability of measurements. The measurement repeatability of the data presented here is calculated as the standard deviation of individual analysis carried out in the reference material UWG-2 over the course of the 2017 and 2020 analytical sessions. SHRIMP–SI $\delta^{18}O$ measurement repeatability for the 2017 and 2020 sessions are 0.43‰ and 0.47‰ (2sd), respectively. The single spot uncertainties derived from the standard deviation

in the primary reference material and the residuals in the calibration curve, added in quadrature to the within-spot uncertainty, are reported in the table below.

After SHRIMP analysis, pits were checked for cracks and irregularities and compromised analyses were discarded. Quantitative WDS spot analyses for an offline oxygen isotope matrix correction were acquired adjacent to SIMS spots on the JEOL 8230 SuperProbe in the Department of Earth Sciences, University of Ottawa and the JEOL 8530F HyperProbe in the Department of Mineral Sciences, Smithsonian Institution National Museum of Natural History. All spot analyses were performed using a 20 kV accelerating voltage, 40 nA current, and 1 μm spot size. Calibrations used multiple natural and synthetic silicate and oxide standards. Matrix corrections for the grossular and spessartine components of garnet analyses were applied following the method detailed in Martin et al (2014). Final isotopic ratios ($^{18}O/^{16}O$) are expressed in delta notation ($\delta^{18}O$ in ‰) relative to VSMOW (Baertschi, 1976).

Garnet name	Session	$\delta^{18}O$ ‰ (SIMS)	2SD ‰	n	$\delta^{18}O$ ‰ (LF)	Bias (total)	Bias (Gross corr.)	$X_{Grossular}$	X_{Pyrope}	$X_{Almandine}$	$X_{Spessartine}$	$X_{Andradite}$
Reference materials used in the grossular matrix-correction:												
UWG2 (primary RM)	2020_August (this work)	5.80	0.43	22	5.80	-		0.14	0.40	0.45	0.01	
UWG2 (primary RM)	2018_July (this work)	5.80	0.47	36	5.80	-		0.14	0.40	0.45	0.01	
UWG2 (primary RM)	2011-2012_All sessions (Martin et al. 2014)	5.80	0.36	91	5.80	-		0.14	0.40	0.45	0.01	
Kakanui	2020_August (this work)	5.50	0.43	15	5.67	-0.17		0.12	0.63	0.23	0.01	0.02
Kakanui	2018_July (this work)	5.36	0.27	18	5.67	-0.31		0.12	0.63	0.23	0.01	0.02
GRS-JH2	2020_August (this work)	21.32	0.38	15	18.70	2.62		0.84		0.01	0.02	0.11
GRS-JH2	2018_July (this work)	21.35	0.30	17	18.70	2.65		0.84		0.01	0.02	0.11
GRS2	2020_August (this work)	9.80	0.41	15	8.01	1.79		0.91				0.07
GRS2	2018_July (this work)	9.99	0.74	18	8.01	1.98		0.91				0.07
GRSSE	2011_September (Martin et al.2014)	4.92	0.51	13	3.80	1.12		0.94		0.04	0.01	
GRSSE	2012_March (Martin et al. 2014)	5.04	0.34	12	3.80	1.24		0.94		0.04	0.01	
GRSSE	2012_May (Martin et al. 2014)	5.06	0.41	12	3.80	1.26		0.94		0.04	0.01	
2B3	2011_September (Martin et al.2014)	7.72	0.44	5	6.90	0.82		0.24	0.03	0.67	0.04	0.02
2B3	2012_March (Martin et al. 2014)	7.97	0.28	12	6.90	1.07		0.24	0.03	0.67	0.04	0.02
2B3	2012_May (Martin et al. 2014)	7.62	0.56	11	6.90	0.72		0.24	0.03	0.67	0.04	0.02
BAL509	2011_September (Martin et al.2014)	11.37	0.48	5	12.30	-0.93		0.03	0.44	0.52	0.01	
BAL509	2012_March (Martin et al. 2014)	11.52	0.48	11	12.30	-0.78		0.03	0.44	0.52	0.01	
BAL509	2012_May (Martin et al. 2014)	11.57	0.67	10	12.30	-0.73		0.03	0.44	0.52	0.01	
PRPAA	2011_September (Martin et al.2014)	5.47	0.47	10	5.50	-0.03		0.11	0.69	0.18	0.01	
PRPAA	2012_March (Martin et al. 2014)	5.19	0.75	11	5.50	-0.31		0.11	0.69	0.18	0.01	
PRPAK	2011_September (Martin et al.2014)	5.51	0.55	10	5.50	0.01		0.11	0.64	0.24	0.01	
PRPAK	2012_March (Martin et al. 2014)	5.13	0.37	12	5.50	-0.37		0.11	0.64	0.24	0.01	
B114	2011_September (Martin et al.2014)	8.39	0.47	10	9.30	-0.91		0.06	0.31	0.61	0.02	
10691	2012_March (Martin et al. 2014)	2.44	0.43	12	0.18	2.26		0.86	0.02	0.05		0.05
10691	2012_May (Martin et al. 2014)	2.58	0.37	11	0.18	2.40		0.86	0.02	0.05		0.05
Reference materials used in the spessartine matrix-correction in addition to UWG2:												
Erongo	2020_August (this work)	9.51	0.42	15	9.30	0.21	1.49	0.02	0.03	0.67	0.28	
Erongo	2018_July (this work)	9.97	0.32	17	9.30	0.67	1.95	0.02	0.03	0.67	0.28	
SPE-BH	2020_August (this work)	10.06	0.66	15	8.13	1.93	2.55	0.07	0.01	0.22	0.68	0.01
SPE-BH	2018_July (this work)	10.39	0.41	18	8.13	2.26	2.89	0.07	0.01	0.22	0.68	0.01
SPE-BH	2012_March (Martin et al. 2014)	10.02	0.58	13	8.13	1.89	2.51	0.07	0.01	0.22	0.68	0.01
SPE-BH	2012_June (Martin et al. 2014)	9.77	0.51	10	8.13	1.64	2.26	0.07	0.01	0.22	0.68	0.01
GRT-1A	2020_August (this work)	11.86	0.43	15	10.12	1.74	3.08	0.01	0.01	0.05	0.93	0.00
GRT-1A	2018_July (this work)	12.26	0.36	17	10.12	2.14	3.48	0.01	0.01	0.05	0.93	0.00
GRT-1A	2012_March (Martin et al. 2014)	11.09	0.31	9	10.12	0.97	2.31	0.01	0.01	0.05	0.93	0.00
GRT-1A	2012_June (Martin et al. 2014)	10.58	0.33	9	10.12	0.46	1.80	0.01	0.01	0.05	0.93	0.00
2B3	2012_March (Martin et al. 2014)	7.97	0.28	12	6.90	1.07	0.05	0.24	0.03	0.67	0.04	0.02

Principal Component Analysis

To robustly assess relationships between major element oscillatory zoning and short length scale fluctuations in $\delta^{18}O$ composition, principal component analysis (PCA) was applied. This approach applies an orthogonal transformation to convert initial variables to a small number of uncorrelated variables. Major element end members (almandine, pyrope, grossular, spessartine, andradite) and the corresponding $\delta^{18}O$ at each SIMS point was included in the analyses, with all transects from each given grain considered together. To preclude dominance of the fractionation-related correlation present in the core of garnet (e.g., negative correlation between $\delta^{18}O$ and spessartine), only analyses across oscillatory rims were considered. To address the effects of closure in compositional (rather than absolute) geochemical data (e.g., Aitchison, 1983), all data were subjected to a centered log-ratio transformation (e.g., Ahmed et al., 2020). To preclude the dominance of high-concentration end-members (i.e., almandine) in PCA results, a z-score transformation was applied to all data. Following data transformations, classical PCA was applied to identify potential groups of overall mass covariance in garnet zoning. The length of each eigenvector in Figure 4 is proportional to the contribution of an element to the principal component; because data have been z-score transformed, these are similar amongst all elements. Eigenvectors that are near-parallel are strongly positively correlated, those at ~90° to each other are uncorrelated, and those ~180° exhibit strong negative correlations. In each case, PC1 and PC2 were found to account for more than ~70% of the variability.

Thermodynamic Modelling

To constrain approximate fluid–rock ratios required to account for large-magnitude $\delta^{18}O$ variations, O-isotope fractionation between thermodynamically stable mineral phases along prograde *P–T* paths were modelled using PTloop (Vho et al., 2020). The strategy incorporated a petrological model using Gibbs energy minimization coupled to an oxygen isotope fractionation model for a given chemical and isotopic bulk rock composition. Phase equilibria were calculated in the MnCKFMASHTO system using the internally consistent dataset of Holland and Powell (1998) and the subsequent ds5.5 update (distributed Feb. 2017). The following activity models were used for the solid solutions: Holland and Powell (2003) for calcite–dolomite–magnesite; Holland and Powell (1998) for garnet, white mica and talc; Holland and Powell (1996) for omphacite; Holland et al. (1998) for chlorite; Diener et al. (2007) for amphibole. Progressive fractionation of garnet from the bulk rock composition was considered along the *P–T* path to simulate the effects of sequestration of garnet-forming components during its crystallization.

The model comprised a single 100 m-thick layer of metabasalt with a bulk composition equivalent to MORB which had undergone extensive seafloor hydration and alteration (Staudigel et al, 1996, Baxter et al., 2013). Starting bulk $\delta^{18}O$ for the metabasalt was set at 14‰, calculated as being in equilibrium with an average garnet core of ~12.5‰ at 480–550 °C. Phase relations and isotope fractionation in altered MORB with an initial $\delta^{18}O$ of 14‰ were simulated along a *P–T* path from 375 °C and 1.4 GPa to 550 °C and 2.0 GPa (Fig. 6A), a path consistent with previously obtained constraints. Equilibrium phase assemblages along this path include lawsonite, and though none has been identified in our Omani samples, numerous authors have documented lawsonite pseudomorphs in garnet in As Sifah eclogites (e.g., El Shazly et al., 2007).

Oxygen isotope fractionation calculations were performed using the database DBOXYGEN 2.0.3 (Vho et al., 2019) at regular intervals with a temperature and pressure spacing of 26 °C and 2.6 MPa. External fluid infiltration into MORB is simulated to occur in a single episode at 500 °C. The oxygen isotope composition of the fluid was simulated to be either serpentinite derived ($\delta^{18}O$=6.7‰) or sediment derived ($\delta^{18}O$=12.5‰). In each case, the fluid mass was constrained to simulate fluid–rock ratios between 0.01 and 6, as needed to reduce the $\delta^{18}O$ to a value equivalent to that observed in the rims of the Omani garnets (9–10.5‰). A third scenario, with no external fluid infiltration but thermal evolution to 595 °C was also simulated to investigate the effects of lawsonite dehydration on the $\delta^{18}O$ of garnet. For Omani samples, this closed-system scenario can be excluded because dehydration of lawsonite was found to release fluid with $\delta^{18}O$ >14‰, too high to account for any significant $\delta^{18}O$ change in garnet (Fig. 6B).

SUPPLEMENTARY MATERIAL 3

Full suite of electron microprobe maps for 16 mapped HP–LT garnets.

CALIFORNIA, UNITED STATES

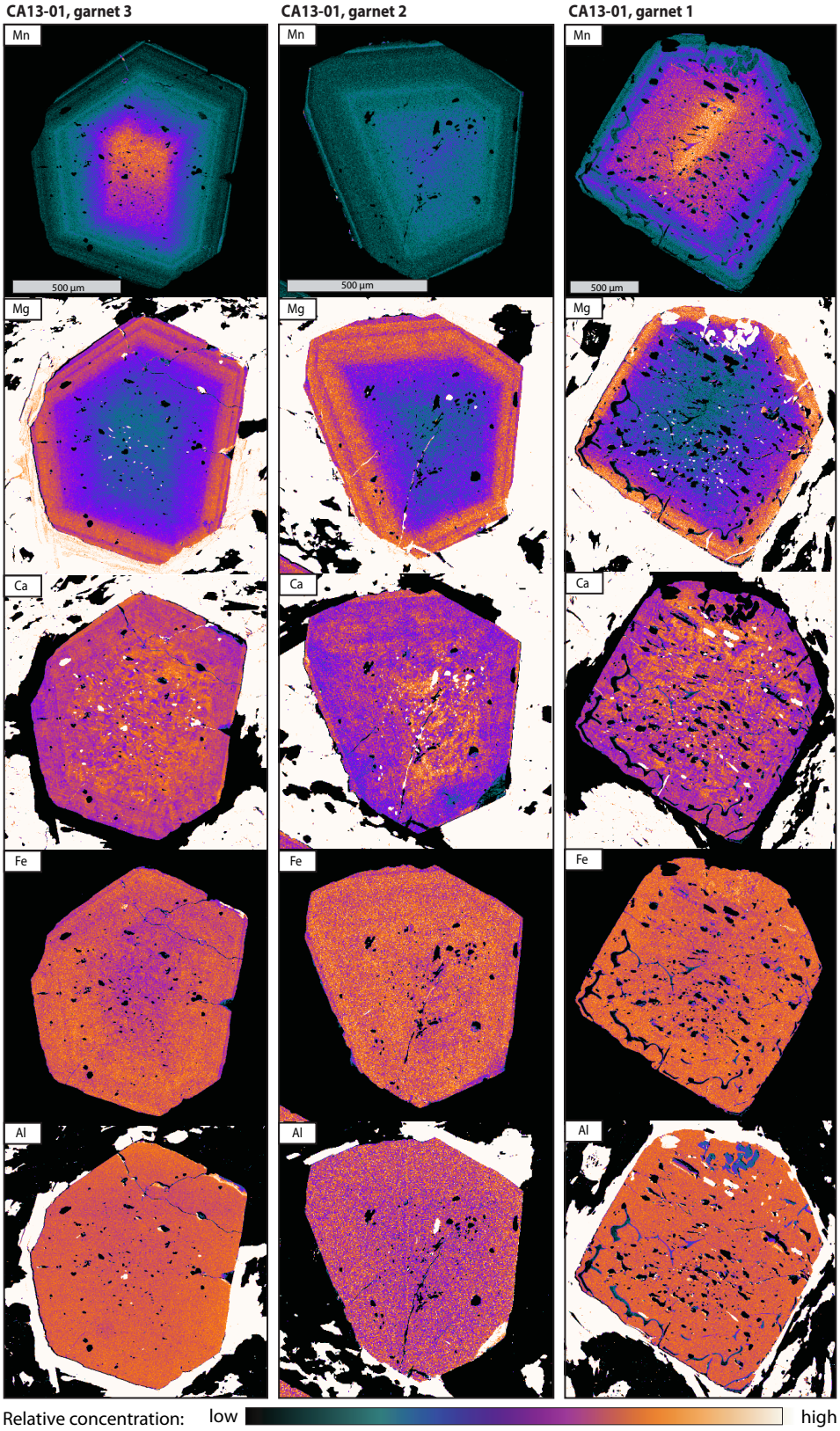

AS SIFAH, OMAN

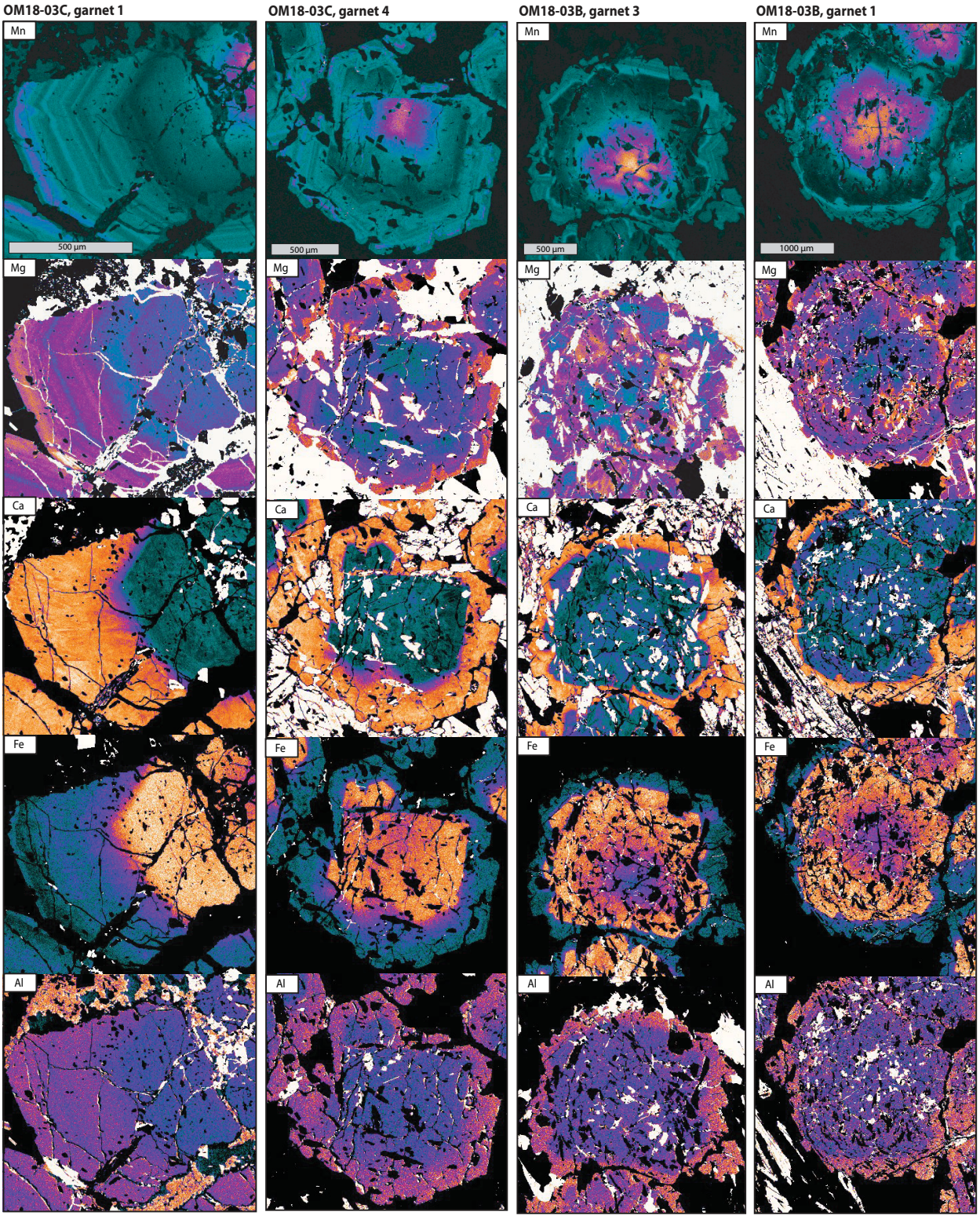

PUERTO CABELLO, VENEZUELA

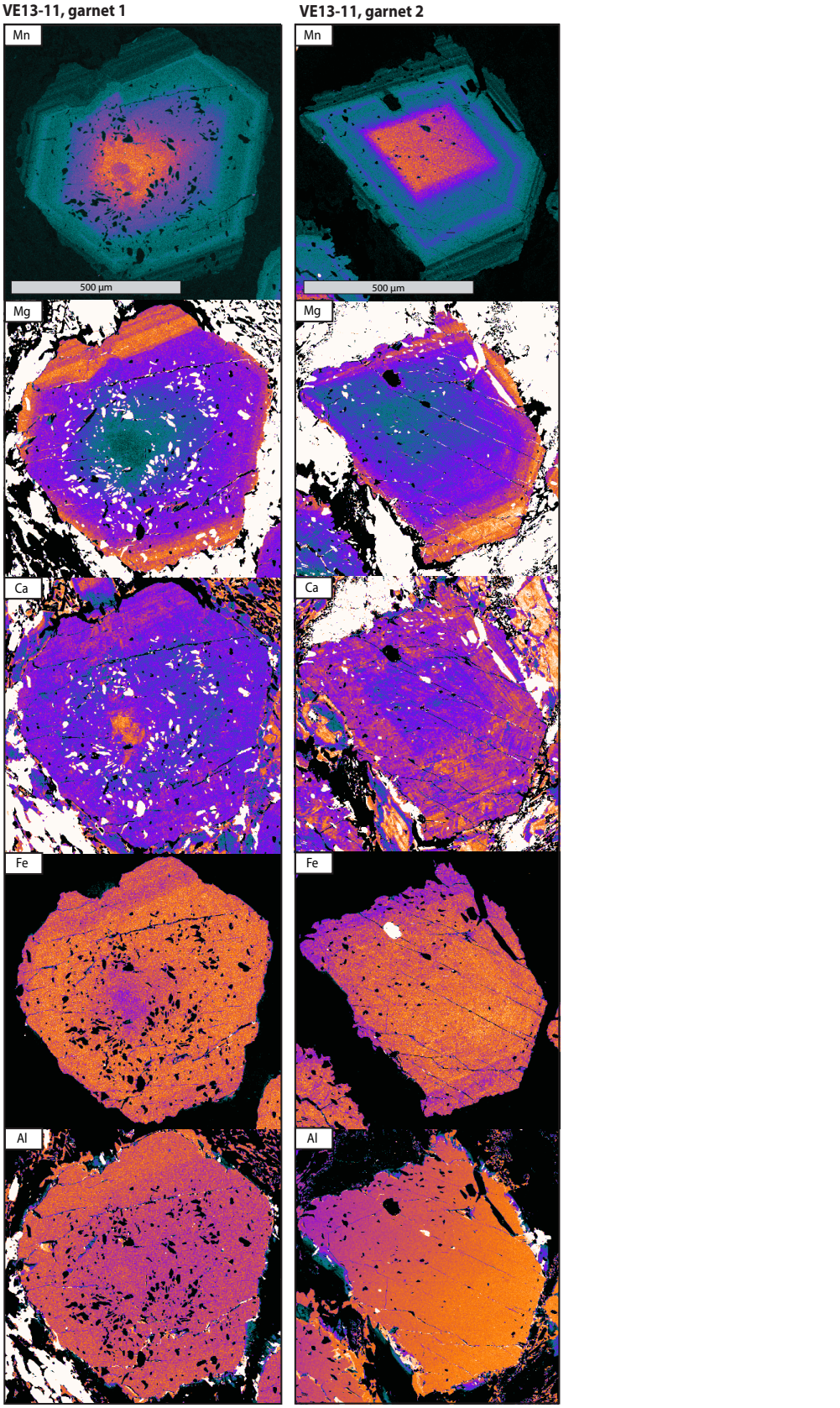

PUNTA BALANDRA, DOMINICAN REPUBLIC

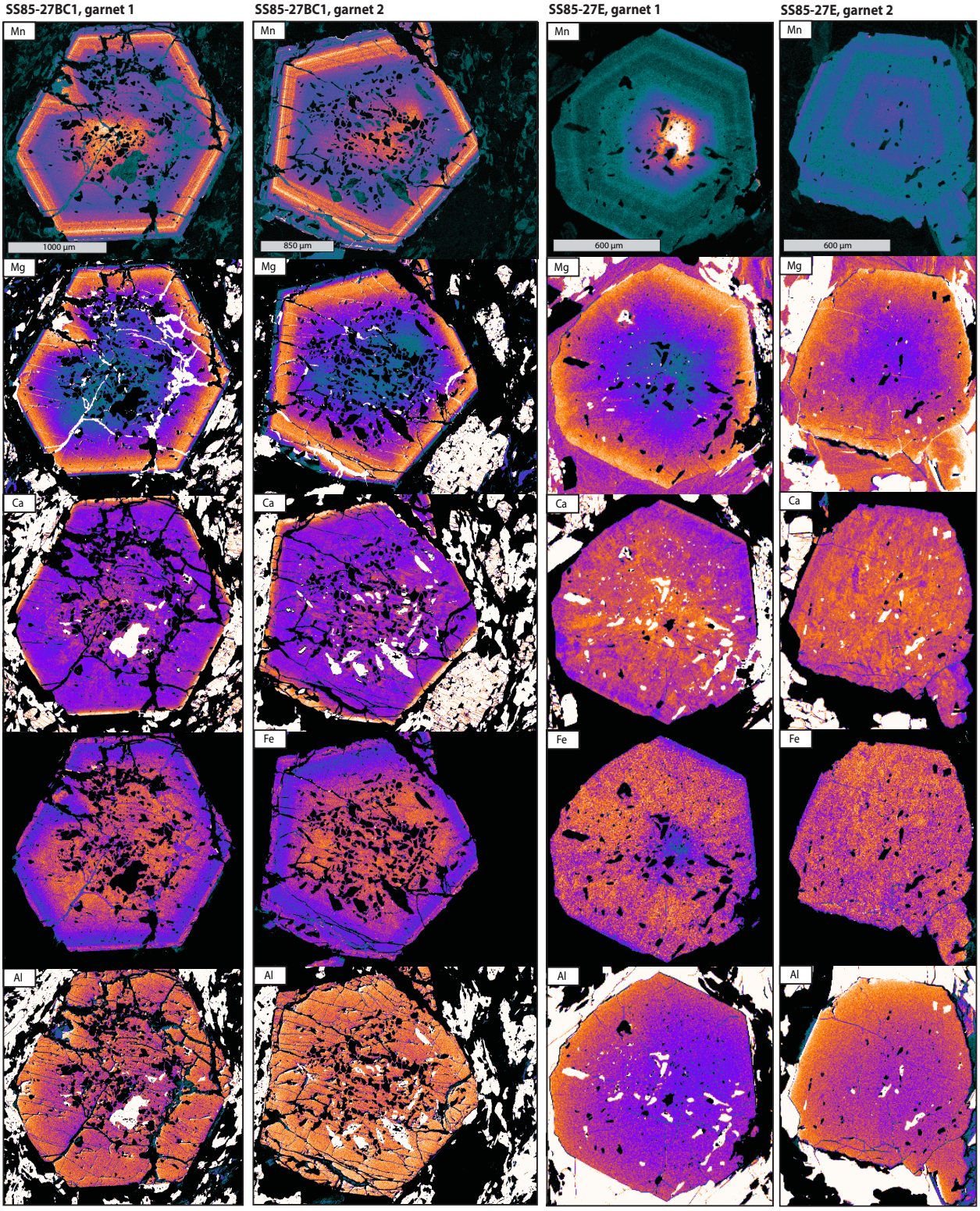

SYROS, GREECE

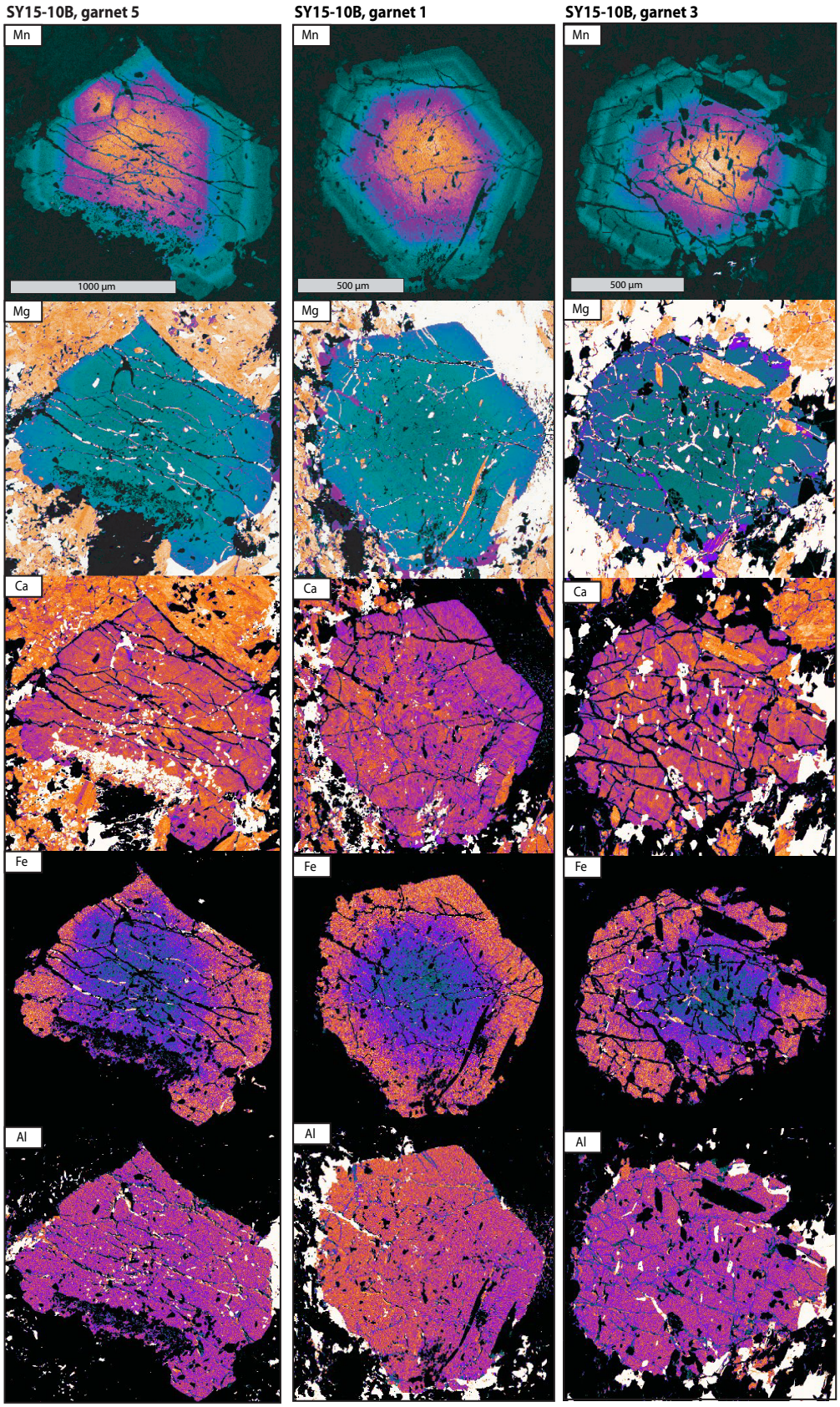

SUPPLEMENTARY MATERIAL 4

LA-ICP-MS raster map of trace elements in garnet from OM18-03C, with associated matrix and inclusions

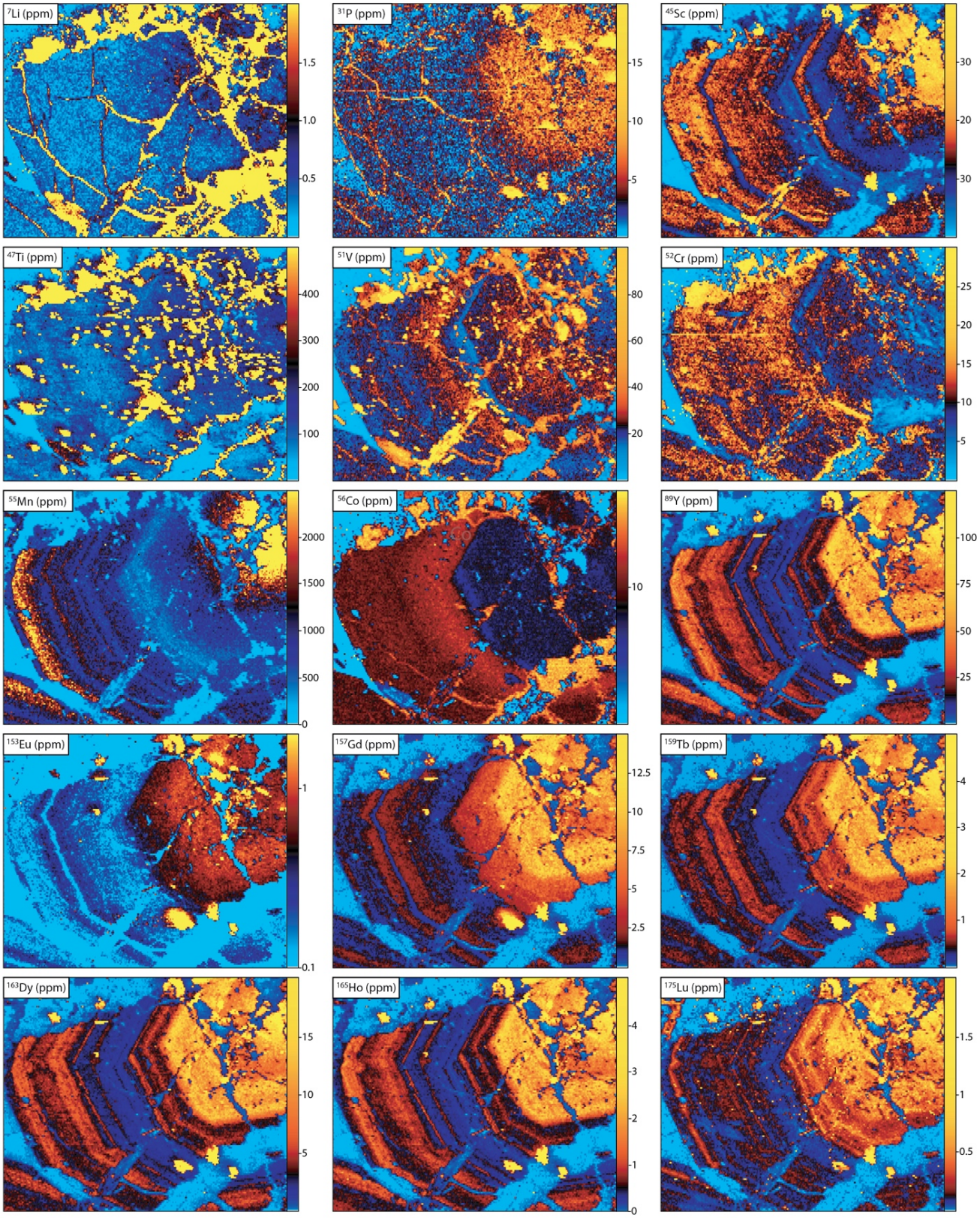

SUPPLEMENTARY MATERIAL 5

Individual EPMA and SIMS measurements for spots in Figures 2 and 4.
Provided as separate .xls file.

REFERENCES

A. D. Ahmed, S. B. Hood, D. R. Cooke, I. Belousov, Unsupervised clustering of LA-ICP-MS raster map data for geological interpretation: A case study using epidote from the Yerington district, Nevada. *Applied Computing and Geosciences*, *8*, 100036 (2020).

J. Aitchison, Principal component analysis of compositional data. *Biometrika*, *70*(1), 57-65 (1983).

J. N. Ávila, T. R. Ireland, P. Holden, P. Lanc, A. Latimore, N. Schram, J. Foster, I. S. Williams, L. Loiselle, B. Fu, High-Precision, High-Accuracy Oxygen Isotope Measurements of Zircon Reference Materials with the SHRIMP-SI. *Geostandards and Geoanalytical Research*, *44*(1), 85-102 (2020)

P. Baertschi, Absolute ^{18}O content of standard mean ocean water. *Earth and Planetary Science Letters*, *31*(3), 341-344 (1976).

E. F. Baxter, M. J. Caddick, Garnet growth as a proxy for progressive subduction zone dehydration. *Geology*, *41*(6), 643-646 (2013).

E. J. Catlos, S. S. Sorensen, Phengite-based chronology of K-and Ba-rich fluid flow in two paleosubduction zones. *Science*, *299*(5603), 92-95 (2003).

J. F. A. Diener, R. Powell, R. W. White, T. J. B. Holland, A new thermodynamic model for clino-and orthoamphiboles in the system Na2O–CaO–FeO–MgO–Al2O3–SiO2–H2O–O. *Journal of Metamorphic Geology*, *25*(6), 631-656 (2007)

K. El-Shazly, R. G. Coleman, J. G. Liou, Eclogites and blueschists from Northeastern Oman: petrology and P-T evolution. *Journal of Petrology*, *31*(3), 629-666 (1990).

K. El-Shazly, M. A. Worthing, J. G. Liou, Interlayered eclogites, blueschists and epidote amphibolites from NE Oman: a record of protolith compositional control and limited fluid infiltration. *Journal of Petrology*, *38*(11), 1461-1487 (1997).

J. Escuder-Viruete, A. Pérez-Estaún, Subduction-related P–T path for eclogites and garnet glaucophanites from the Samana Peninsula basement complex, northern Hispaniola. *International Journal of Earth Sciences*, *95*(6), 995-1017 (2006).

P. Goncalves, S. Guillot, J. M. Lardeaux, C. Nicollet, B. Mercier de Lepinay, Thrusting and sinistral wrenching in a pre-Eocene HP-LT Caribbean accretionary wedge (Samaná Peninsula, Dominican Republic). *Geodinamica acta*, *13*(2-3), 119-132 (2000).

J. Hellstrom, C. Paton, J. Woodhead, J. Hergt, Iolite: software for spatially resolved LA-(quad and MC) ICPMS analysis. *Mineralogical Association of Canada short course series*, *40*, 343-348 (2008).

T. J. B. Holland, R. T. J. B. Powell, An internally consistent thermodynamic data set for phases of petrological interest. *Journal of metamorphic Geology*, *16*(3), 309-343 (1998).

T. J. B. Holland, R. T. J. B. Powell. Thermodynamics of order-disorder in minerals; I, Symmetric formalism applied to minerals of fixed composition. *American Mineralogist*, *81*(11-12), 1413-1424 (1996)

T. J. B. Holland, R. T. J. B. Powell, Activity–composition relations for phases in petrological calculations: an asymmetric multicomponent formulation. *Contributions to Mineralogy and Petrology*, *145*, 492-501 (2003)

L. A. Martin, D. Rubatto, C. Crépisson, J. Hermann, B. Putlitz, A. Vitale-Brovarone, Garnet oxygen analysis by SHRIMP-SI: Matrix corrections and application to high-pressure metasomatic rocks from Alpine Corsica. *Chemical geology*, *374*, 25-36 (2014).

C. Paton, J. Hellstrom, B. Paul, J. Woodhead, J. Hergt, Iolite: Freeware for the visualisation and processing of mass spectrometric data. *Journal of Analytical Atomic Spectrometry*, *26*(12), 2508-2518 (2011).

B. Putlitz, M. A. Cosca, J. C. Schumacher, Prograde mica 40Ar/39Ar growth ages recorded in high pressure rocks (Syros, Cyclades, Greece). *Chemical Geology*, *214*(1-2), 79-98, (2005).

R. J. Quinn, J. W. Valley, F. Z. Page, J. H. Fournelle, Accurate determination of ferric iron in garnets. *American Mineralogist*, *101*(7), 1704-1707 (2016).

K. Ravna, The garnet–clinopyroxene Fe2+–Mg geothermometer: an updated calibration. *Journal of metamorphic Geology*, *18*(2), 211-219 (2000).

V. B. Sisson, I. E. Ertan, H. G. A. Lallemant, High-pressure (~2000 MPa) kyanite-and glaucophane-bearing pelitic schist and eclogite from Cordillera de la Costa belt, Venezuela. *Journal of Petrology*, *38*(1), 65-83 (1997).

H. Staudigel, T. Plank, T. B. White, H. U. Schmincke, Geochemical fluxes during seafloor alteration of the basaltic upper oceanic crust: DSDP Sites 417 and 418. *Subduction: top to bottom*, *96*, 19-38 (1996).

F. Trotet, L. Jolivet, O. Vidal, Tectono-metamorphic evolution of Syros and Sifnos islands (Cyclades, Greece). *Tectonophysics*, *338*(2), 179-206 (2001).

T. Tsujimori, K. Matsumoto, J. Wakabayashi, J. G. Liou, Franciscan eclogite revisited: Reevaluation of the P–T evolution of tectonic blocks from Tiburon Peninsula, California, USA. *Mineralogy and Petrology*, *88*(1-2), 243 (2006).

J. W. Valley, N. Kitchen, M. J. Kohn, C. R. Niendorf, M. J. Spicuzza, UWG-2, a garnet standard for oxygen isotope ratios: strategies for high precision and accuracy with laser heating. *Geochimica et Cosmochimica Acta*, *59*(24), 5223-5231 (1995).

A. Vho, P. Lanari, D. Rubatto, An internally-consistent database for oxygen isotope fractionation between minerals. *Journal of petrology*, *60*(11), 2101-2129 (2019).

A. Vho, P. Lanari, D. Rubatto, J. Hermann, Tracing fluid transfers in subduction zones: an integrated thermodynamic and $\delta^{18}O$ fractionation modelling approach. *Solid Earth*, *11*(2), 307-328 (2020).

D. R. Viete, B. R. Hacker, M. B. Allen, G. G. Seward, M. J. Tobin, C. S. Kelley, G. Cinque, A. R. Duckworth, Metamorphic records of multiple seismic cycles during subduction. *Science advances*, *4*(3), eaaq0234 (2018).

D. J. Waters, The garnet-clinopyroxene-phengite barometer. In *Terra Abstract*, 5, 410-411 (1993).